Structural and physical properties of ReNiO$_3$ (Re=Sm, Nd) nanostructured films prepared by Pulsed Laser Deposition

BY

Ngom, Balla Diop

Thesis presented in fulfilment of the requirements for the degree of Ph.D in Physics in the Faculty of Science, University of the Western Cape (UWC)

Supervisor: Prof M. Maaza
Nanosciences Laboratories, Materials Research Department, iThemba LABS, National Research Foundation, South Africa,

Co-supervisor: Prof R. Madjoe
Department of Physics, Faculty of Science, University of the Western Cape, Cape Town, South Africa,

April 2010

ACKNOWLEDGEMENTS:

I would like to express my appreciation to:

1 Prof M Maaza, Materials Research Department, iThemba LABS, for his guidance and supervision throughout the project.

2 Prof. R Madjoe, Departement of physics University of the Western Cape, for his guidance and supervision throughout the project.

3 Prof A C BEYE, Universite Cheikh Anta Diop de Dakar, for the interest he maintained throughout this study as supervisor.

4 Dr. Z. Z. Vilakazi, Director of iThemba LABS, for his encouragement and making possible the use of facilities at the iThemba LABS.

5 Dr. R. Nemtudi Materials Research Department, iThemba LABS, who acted as co-supervisor gave guidance, and advise during many discussions throughout my study.

6 Dr Ncholu Manyala throughout many discussions on the project.

7 Dr A. Y. Fasasi throughout many discussions on the project.

8 Dr O. Nemraoui throughout many discussions on the project.

9 Dr. Remy throughout many discussions on the project.

10 Dr. A. Forbes throughout many discussions on the project and hosting me at the NLC, making the PLD available for me.

11 Special Thanks to Prof Phillip Lacorre; Prof A. Ambrosini and Prof Maria Luisa Medarde, for the e-mail exchanging and for making your expertise and your work available for me during this Ph.D work.

12 My parents and family for their support.

13 Mame Marietou (Minia), je t'aime fortement, thanks for your love and trust.

14 The staff and students at the Materials Research Department, iThemba LABS.

15 D. Smith and Callie for their Support.

UNIVERSITY *of the*

WESTERN CAPE

I dedicate this thesis to my parents for their undying love, support and trust.

through the formation of the shock wave. On the basis of these data it has to be noticed that this estimate morphology feature where all films show a similar behavior as a function of pressure, can be related into the diffusion of the plasma species as the films were deposited at distance above the estimated stopping distance of the plasma.

List of Tables

CHAPTER I

1. Introduction

1.1 Background

Very few systems allow the study of the relationship between structural changes and physical properties in such a clear way as rare earth nickelate $ReNiO_3$ perovskites (Re (rare earth) = Pr, Nd, Sm and Gd). Synthesized for the first time by Demazeau et al [1] in 1971 and completely forgotten for almost twenty years, these compounds have regained interest since the discovery of high-temperature superconductivity and giant magnetoresistive effects in other perovskite-related systems. Although the nickelates do not display any of these exotic properties, they are, together with cuprates and manganites, one of the rare families of oxides which show good metallic conductivity.

Similarly to the standard Mott type oxides, these so called nickelate materials of the family $ReNiO_3$ which have been studied during the previous decade in their bulk form [1-11] display a noteworthy Metal-Insulator Transition (MIT) that is from a specific and innovative significance for novel nanophotonics such as tunable Infrared modulation photonics and ultra-fast optical switchings for high power laser sources and intense infrared fluences.

Due to its Metal–Insulator Transition (MIT) and thermochromic properties, the rare earth nickelate perovskite $ReNiO_3$ has received a great deal of attention for the past ten years in their thin films form [12]. Such unusual electronic and optical features are all the more interesting since the metal–insulator transition temperature (T_{MIT}) can be tuned by changing the Re cation: $LaNiO_3$ is metallic

1
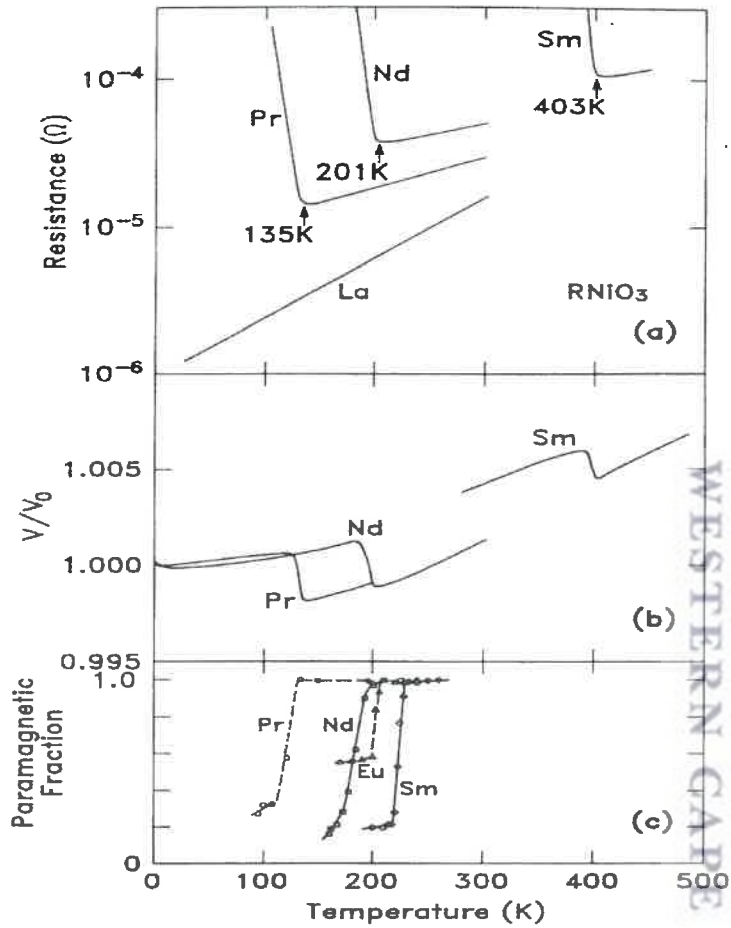
Figure 1.1

Figure 1.2

(a) The electrical resistance of $LaNiO_3$, $PrNiO_3$, $NdNiO_3$ and $SmNiO_3$ showing their metal–insulator transitions (MIT). (b) The temperature dependence of the relative unit cell volume showing the anomaly at MIT. (c) The paramagnetic fraction as determined from muon$^+$ spin rotation experiments, which drops suddenly at the antiferromagnetic ordering temperature [3].
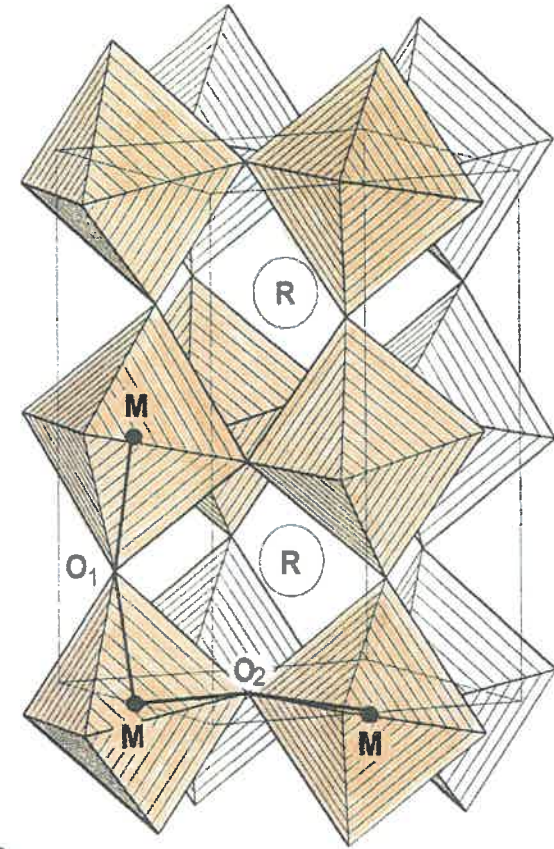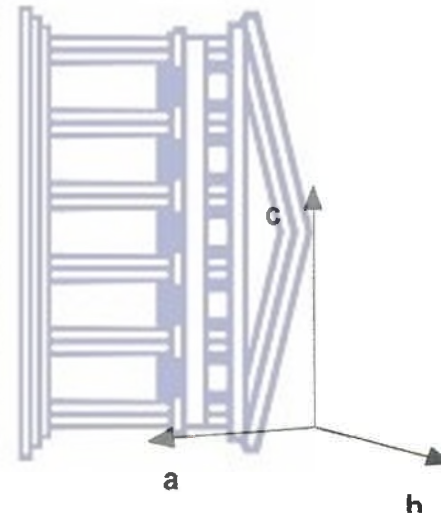
Orthorhombic perovskite structure.

No minimum of the metallic conductivity of $Sm_{0.55}Nd_{0.45}NiO_3$, as observed by Gire et al [12] (entropic effect), was reported by Ambrosini and Hamet [11].

It has been suggested by Obradors et al. [13] that changing the rare earth cation in the $ReNiO_3$ system, acts as internal chemical pressure (increasing internal pressure by substituting the rare earth cation with another one of larger ionic radius) which can lead, as for the isostatic pressure experiment, to a tunability of the metal–insulator transition temperature [14, 15]. Obradors et al [13] reported on a decrease of T_{MIT} upon increasing isostatic pressure but with remaining metallic properties of $PrNiO_3$ and $NdNiO_3$ (same magnitude and thermal dependence of the electrical resistivity). Canfield et al [14] observed the same phenomenon with only a slight decrease of the metallic resistivity upon elevating external pressure. The effect of the external pressure was directly correlated to the variation of the tolerance factor: an increasing pressure increases the tolerance factor and decreases T_{MIT}. But, as pointed out by Medarde et al [15], the analogy is not simple since controversial conclusions are proposed by Canfield et al and Obradors et al who respectively found a negative [14] and positive [13] value for the external pressure (Pext) dependence of the tilt angle w ($\partial w / \partial$ Pext). A more recent structural investigation of Medarde et al [15] has revealed clear difference between internal and external pressure and in particular underlined that in the internal pressure mechanism the angle tilting is the most affected parameter compared to the variation of the Ni–O bond length.

The superior advantage of these nickelate materials $ReNiO_3$, relatively to the standard MIT Mott type oxides such as vanadium oxides, is the controllability of their T_{MIT}. The shift of their T_{MIT} can be precisely regulated by the choice of the lanthanide cation; a smaller cation induces a distortion of the Ni-O-Ni angle from 180°, and therefore the metal-insulator occurs at higher temperature. This remarkable property of these high temperature stable perovskites in the ability to

5

Sample	Composition "x"	Transition temp. T_{MIT} "°C"
$Sm_{1-X}Nd_XNiO_3$	0.9	-53
"	0.75	-23
"	0.6	7
"	0.5	27
"	0.45	37
"	0.425	42
"	035	57
"	0.25	77
"	0.10	107

Table 1.1

Metal-Insulator Transition Temperature (T_{MIT}) dependence of the composition of the solid solution $Sm_{1-X}Nd_XNiO_3$.

7

In Chapter III the pulsed laser ablation phenomenon is discussed in details, from the laser–target interaction, through the plasma formation and expansion, up to the film nucleation and growth.

In Chapter IV the details of PLD instrumental endowment and the descriptions of the various analysis techniques used are reported.

The results obtained by monitoring the film growth for each value of deposition parameters investigated by mean of the characterization techniques, were interpreted by means of the results on plume expansion dynamics by time gated fast photography technique, are reported on Chapter V as well as the discussions of the results.

The cross-correlation between the experimental results, obtained using complementary techniques focusing on the two distinct fundamental stages of the laser deposition process, such as the plume expansion and the film growth as well as future work, are discussed in the conclusion section, this is reported in chapter VI.
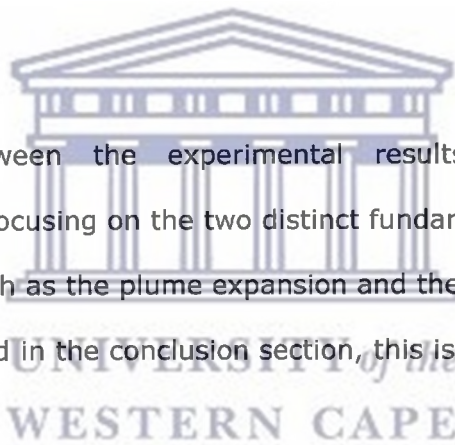
1.5 Bibliography

[1]   D D Sarma & al. Phys.: Condens. Matter 6 (1994) 10467-10474.

[2]   J. L. Garcia-Munoz & al. 1992 Phys. Rev. B 46 4414.

[3]   P. Lacorre & al 1991 J. Solid State Chem. 91 225.

[4]   F. Bartolome & al. J. of Appl. Phys. 87 (2000) 7052-7054.

[5]   E. Nestor & al. Phys. Review B 56 (1997) pp 986-988.

[6]   G. Demazeau & al. J. Solid State Chem. 3 (1971) 582.

[7]   J. Blasco & al. Phys.: Condens. Matter 6 (1994) 10759-10772.

CHAPTER II

2. GENERAL PROPERTIES OF RENIO3 (RE =RARE EARTH) COMPOUNDS

$ReNiO_3$ perovskites (Re = rare earth) provide a remarkable opportunity to study the relationship between structural and physical properties since, by moving along the 4f rare earth series, the evolution of several transport and magnetic properties can be nicely correlated to the steric effects associated with the lanthanide contraction. The most appealing example is probably the metal–insulator transition discovered for the compounds with Re except La, whose critical temperature MIT increases with decreasing size of the rare earth ion.

On the other hand, several experimental results show that in $ReNiO_3$ perovskites the degree of Ni 3d–O 2p hybridization is extremely high. The purely ionic (Ni^{3+} O^{2-}) configuration, first suggested by neutron diffraction experiments, has been then substituted by a ground state where the $3d^7 2p^6$ (Ni^{3+} O^{2-}) and $3d^8 L$ (Ni^{2+} O^-) configurations are strongly mixed.

In this chapter, a summary of the scientific work performed on the $ReNiO_3$ system during the last years is presented. The results of the different experimental techniques are successively reviewed, with special emphasis on the relationship between the structural and the physical properties. The possible mechanisms responsible for the metal–insulator transition, which is still a major open question for $ReNiO_3$ bulk perovskites, are also discussed.

2.1 Methods of preparing ReNiO₃ bulk and films.

2.1.1 ReNiO₃ bulk synthesis

11

Recently, alternative procedures have been described by different authors [2, 3]. The major interest of these new methods of synthesis is the fact that only moderate oxygen pressures and/or temperatures are needed. Thus, Vassiliou et al [2] succeeded in preparing NdNiO$_3$ at 650 ^{o}C in 1 bar oxygen, and Lacorre *et al* [3] were able to obtain LaNiO$_3$, PrNiO$_3$, NdNiO$_3$, SmNiO$_3$ and EuNiO$_3$ at 1000 ^{o}C and 150–200 bar. Other important advantages are (i) the better availability of the equipment, (ii) the possibility of producing larger amounts of sample and (iii) the availability of samples as sintered pellets, which is very convenient for performing transport measurements.

2.1.2 ReNiO$_3$ thin films synthesis

There were many techniques which have been subjected to optimizations. The experiment techniques which have been employed include: Chemical vapour deposition (CVD) [4], Magnetron sputtering [5, 6], Sol-gel process [7], and Pulsed laser deposition (PLD) [8].

2.1.2.1 Chemical Vapour Deposition Method

Chemical Vapor Deposition (CVD) is known as a method growing films at relatively high temperature. The charged and neutral particles that formed during the production of the films by CVD are normally moved randomly and they are often electrical neutral on average [9].

The production of ReNiO$_3$ films using CVD is possible if the substrate has impact energies ranging from 50eV to < 1000eV. At the bias voltage of about (-100V), ReNiO$_3$ films doesn't depend upon the sources [4]. The reagents formed as a result of the volatile chemical vapour reaction between the precursors are decomposed and grown onto the substrate heated to high temperature.

applications such as decorative, wear resistant, optical and magnetic thin films. It has proven to be a superior method of coating a variety of substrates thin films of electrically conductive or non conductive materials. Direct current (DC) sputtering is used to sputter conductive materials; while radio-frequency is used to sputter non-conductive materials [11].

Several researchers have used these techniques for preparation of ReNiO$_3$ thin films. P. Laffez *et al* have used DC reactive sputtering for depositing ReNiO$_3$ thin films, which is the most standard method [6]. This technique is characterized by the features which are much interesting for industrial applications i.e. high deposition is possible and the composition of films is controllable [12]. Authors like Chu et al [13], have used the RF magnetron sputtering. In the RF-sputtering, the RF-energy is applied to the surface of the target and is capacitively coupled to the front surface [11].

2.1.2.3 Sol-gel Method

Sol gel process is the method which is frequently used to synthesize nanophase metal oxide particles in a colloidal suspension. In general, the sol-gel process involves the transition of a system from a liquid solution "sol" (mostly colloidal) into a solid "gel" phase. This process is very promising for the formation of metal oxides and temperature sensitive organic hybrids, nanocomposites which allow molecular level composition homogeneity. It provides excellent precursor chemistry and processing conditions and, also provides excellent chemical homogeneity metastable structure at low reaction temperatures [14].

In a typical sol-gel process, the precursor is subjected to a series of hydrolysis and polymerization reactions to form a colloidal suspension, or a "sol". Further processing of the "sol" enables one to make ceramic materials in different forms. Metal oxides are useful precursors for the synthesis of the oxides [15].

15

discovery of periodic mesoporous silica such as Mobile Crystalline Material was reported [16].

2.1.2.4 Pulsed Laser Deposition (PLD) Method

This study is mainly focusing on the films grown by PLD, which is also known as a technique with ability to grow complex materials in high-Temperature high-pressure and ceramic coatings using different lasers.

In the PLD method the laser beam is generated from the laser source (Lambda Physik). There are several instruments used to direct the laser beam direct towards the surface of the solid target. The interaction of the laser radiation and target breaks the chemical bond in the target material to produce particulates containing atoms, ions, electrons, molecules, atomic clusters and larger particulates. The ablated particulates form a plasma plume and expand in the vacuum chamber and accelerate directly towards the surface the substrate to form films.
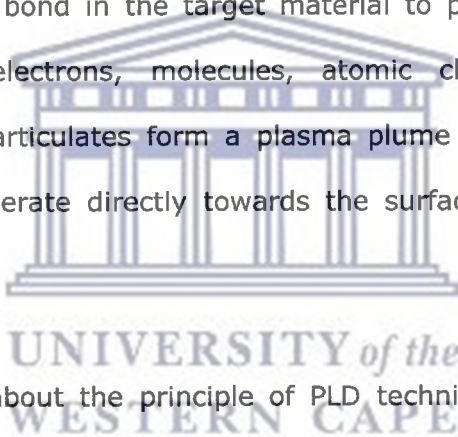
More detailed information about the principle of PLD technique, which is used during the preparation of this thesis, will be given in chapter III.

2.2 Crystal structures

2.2.1 Introduction

From the structural point of view, the ReNiO₃ compounds are orthorhombically distorted perovskites [9]. The aristotype of this structural family, whose chemical formula can be written in a general way as ABX_3, is the mineral 'perovskite' ($CaTiO_3$). The ideal cubic structure, which is displayed by $CaTiO_3$ above 900 °C (see figure 2.1(a)), consists of a 3D array of corner-sharing BX_6 octahedra, located at the nodes of a simple cubic lattice. At the centre of the unit cell ((1/2

17

In figure 2.2 we have represented the variation of the lattice parameters as a function of the tolerance factor. From this picture we deduce that the orthorhombic distortion, which becomes more important with decreasing radius of the rare earth ion, is stable from $t \approx 0.932$ (Lu) to $t \approx 0.975$ (Pr). In the case of LaNiO$_3$, the high value of the tolerance factor ($t \approx 0.986$) allows the less distorted rhombohedral structure to be stabilized. The boundary between these two phases has been situated by Lacorre et al at $t \approx 0.985$ [3].

An interesting trend, which has been observed in all the presently available nickelates (from LaNiO$_3$ to EuNiO$_3$) is the practical invariance of the average Ni−O distance (see table 2.1). The NiO$_6$ octahedra behave approximately as rigid bodies, the departure from the ideal perovskite structure along the series being due to their cooperative tilts. The cosine of the tilt angle ϖ is, to a first approximation, a linear function of T$_{MIT}$ [23]. Although this tendency has to be tested for the remaining nickelates, it strongly suggests that this angle is the relevant structural parameter controlling the evolution of MIT along the series.

2.2.3 The structural phase transition

Figure 1.1 (b) (Chapter 1) shows the thermal evolution of the relative unit cell volume $V=V_0$ (V_0 is the volume at 1.5 K) for PrNiO$_3$, NdNiO$_3$ and SmNiO$_3$. These measurements clearly show the existence of a sudden (first-order), small expansion of the unit cell (about 0.2%) at the temperature where the MIT takes place.

The variation of the unit cell volume is the result of a small increase in the Ni−O distance ($\approx 0.2\%$) and a simultaneous decrease of the Ni−O−Ni superexchange angle θ ($\approx 0.4\%$, see figure 2.3). Here, θ is defined as $\theta \approx \pi - 2\varpi$, where ϖ is the tilt angle of the NiO$_6$ octahedra.

19
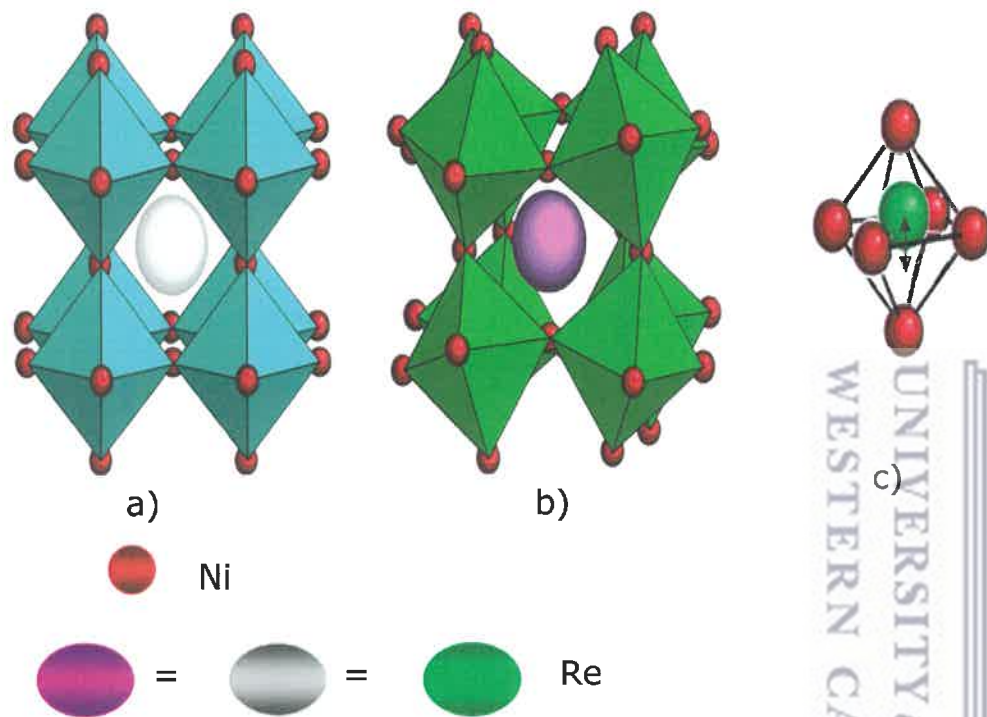
Figure 2.1

(a) The ideal perovskite structure (cubic Pm3m). (b) Rhombohedral distortion (R3c). (c) Ortho-rhombic distortion (Pbnm).
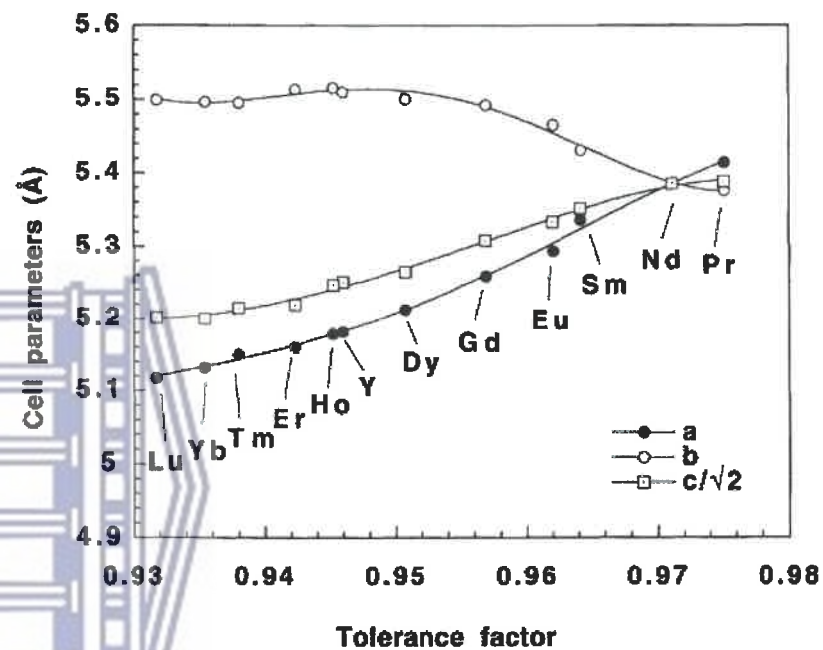
Figure 2.2

The variation of the lattice parameters as a function of the tolerance factor in the ReNiO₃ series. The values of t have been calculated by using $d_{Ni-O} = 1.94$ Å (the same for all the nickelates) and the R–O distances given in [24] for trivalent rare earth ions in coordination 12.
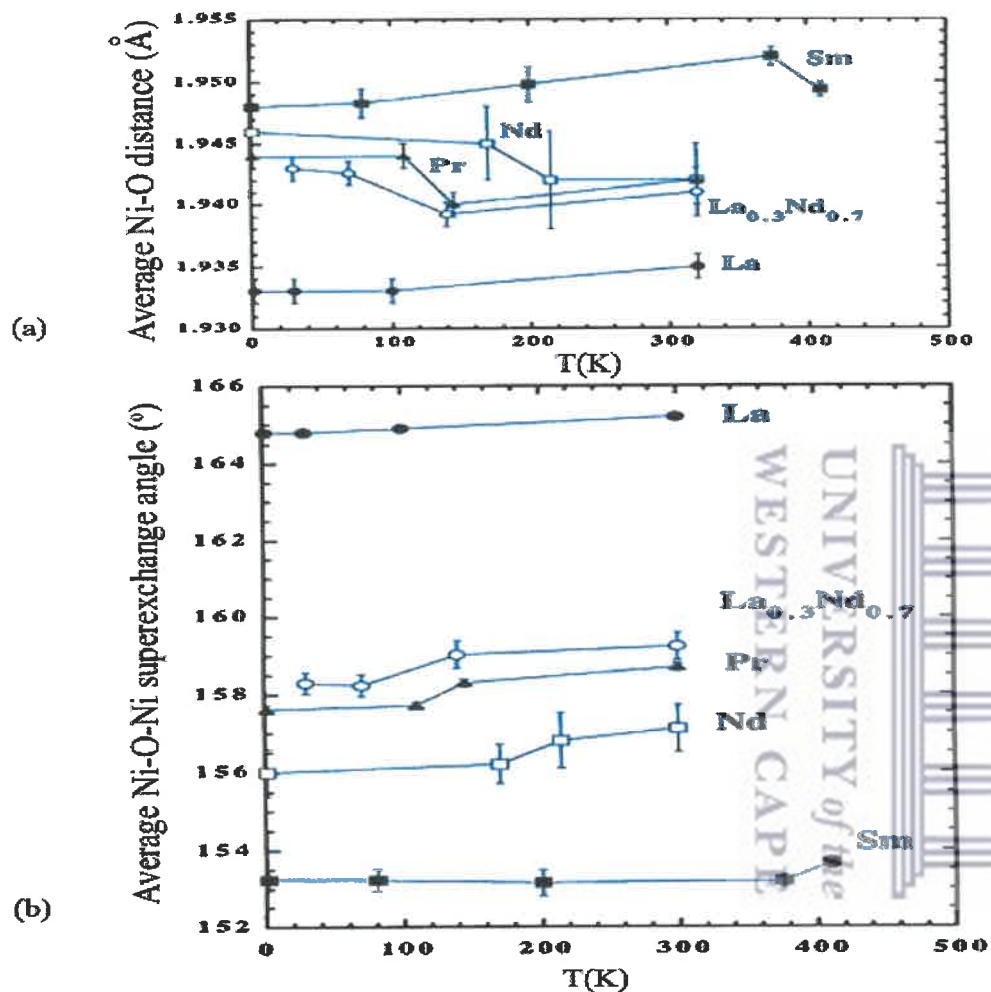
Figure 2.3

The thermal evolution of (a) the average Ni–O distance and (b) the average Ni–O–Ni angle for the nickelates with R = La, Pr, Nd [4], Sm [25] and $La_{0.3}Nd_{0.7}$ [26].
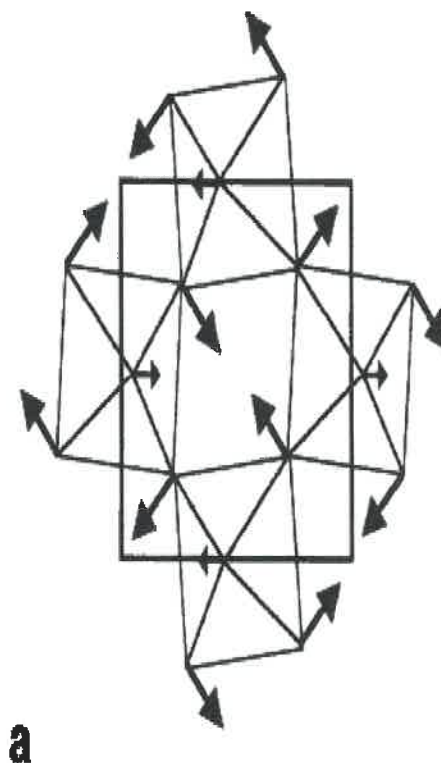
Figure 2.4

A scheme of the atomic displacements across the M–I transition (adapted from [15]).

2.3.2 The Seebeck coefficient

The nature of the carriers can be deduced from the sign of the Seebeck coefficient S (T). Its thermal behaviour, which is displayed in figure 2.5(a) for PrNiO$_3$, shows a linear dependence for T > MIT. Moreover, it is small in magnitude and negative ($\approx -10 \ \mu$V K^{-1}). These values are typical for a metal with e$^-$-like particles as charge carriers. Assuming a simple free-electron model, the observed slope of S (T) in the metallic regime indicates an effective charge concentration of about 4.6x10^{20} e$^-$.cm^{-3}, that is, 0.025 e$^-$/Ni atom.

If we compare this result with the effective electron densities of pure 3d transition metals (see for example [32]), we find a difference of about two orders of magnitude. ReNiO$_3$ perovskites are, then, very bad metals. Even if this is only a very qualitative argument, this fact would explain the smallness of some of the effects (the structural changes or the variation of the density of states) observed at the T$_{MIT}$.

As expected across an MIT, S (T) decreases abruptly below T$_{MIT}$, becoming very large in magnitude ($S= -270 \ \mu$V K^{-1} at 77 K). However, its sign is always negative, thus indicating that carriers are also electrons in the insulating state.

2.3.3 Hysteresis across the metal–insulator transition

Due to the first-order nature of the T$_{MIT}$, a coexistence of the high-temperature metallic phase and the low-temperature insulating phase over a certain temperature range close to MIT could be expected, thus leading to a hysteretic behaviour of the transport properties.

Figure 2.5 shows the Seebeck coefficient and the resistance of PrNiO$_3$ measured in a cooling–heating cycle [27], where this hysteretic behaviour is clearly observed. Notice that the upper and lower limits of the hysteretic region (T$_{MIT}$ and

25
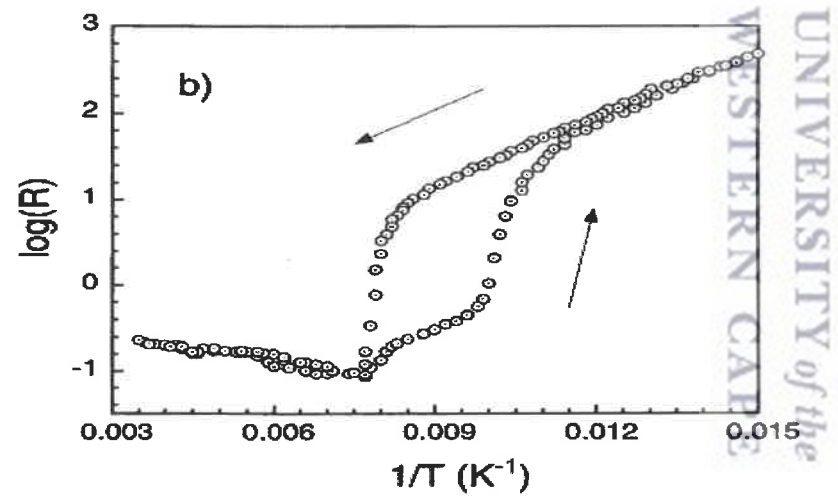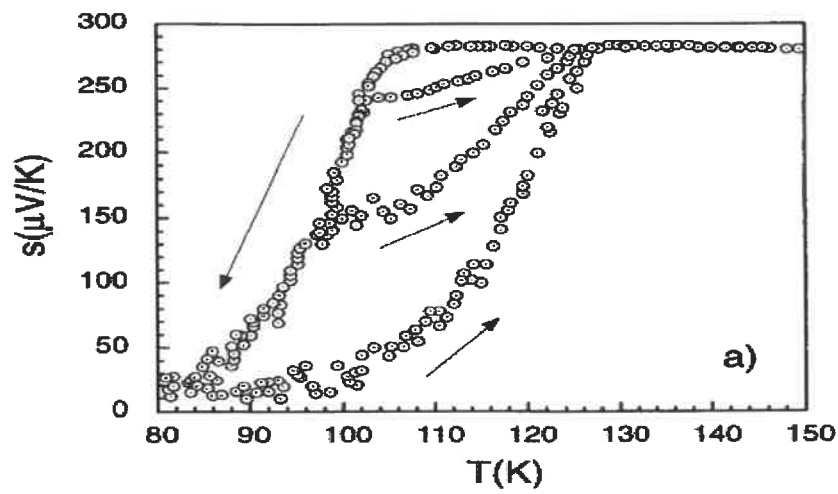
Figure 2.5

The hysteresis below T_{MIT} = 130 K in (a) the Seebeck coefficient and (b) the electrical resistance of $PrNiO_3$ [27].
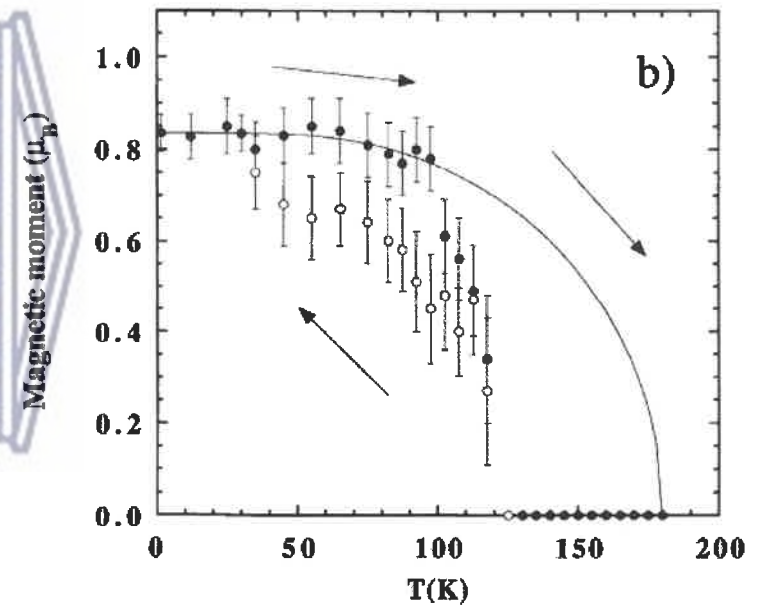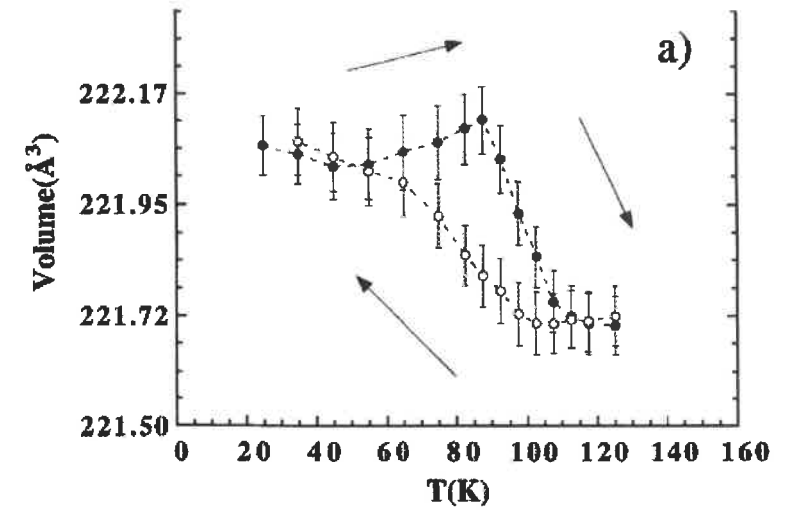
Figure 2.6

The hysteresis below T_{MIT} = 104 K in the unit cell volume and the Ni magnetic moment of $La_{0.3}Nd_{0.7}NiO_3$ [1].

27
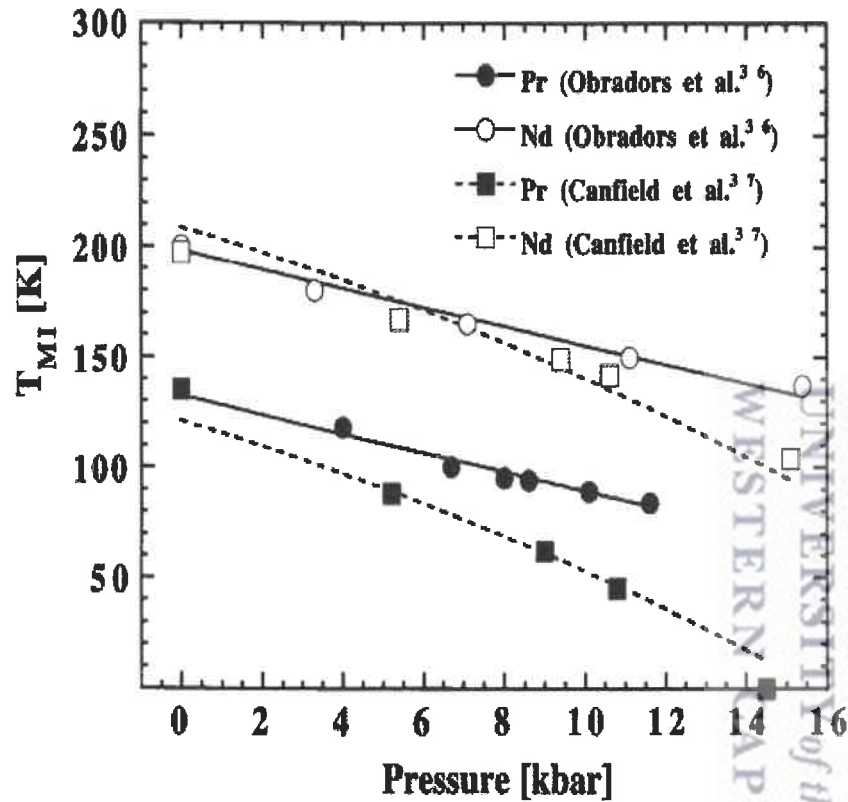
Figure 2.7

The pressure dependence of T_{MIT} ([33, 34]).
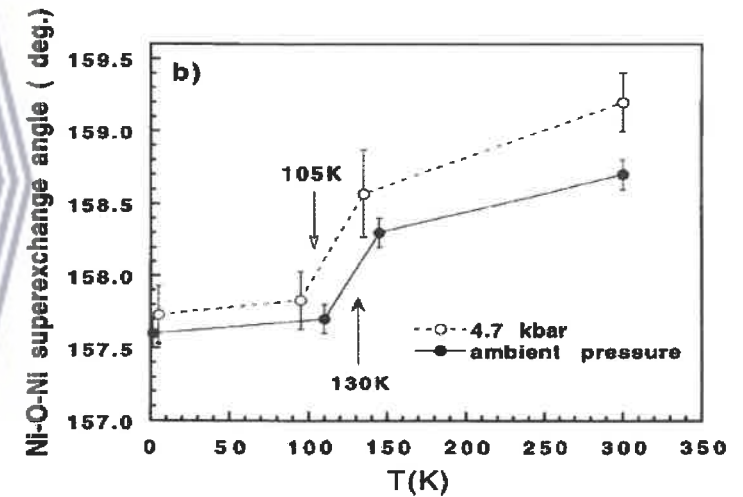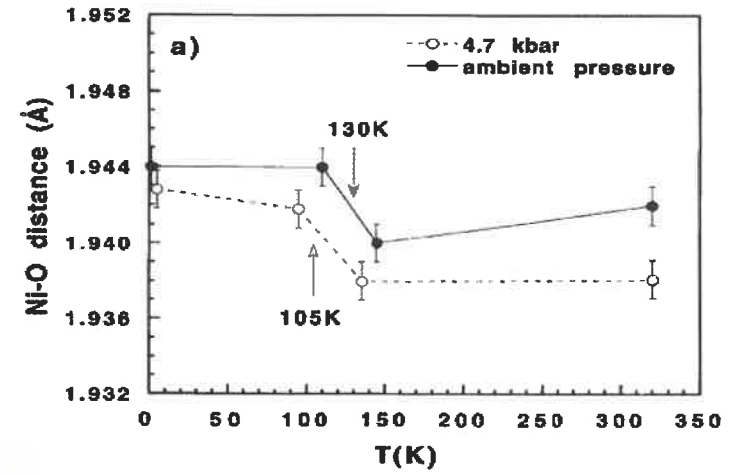
Figure 2.8

The pressure dependences of the average Ni–O distance and the average Ni–O–Ni angle in PrNiO3 [35].

An alternative, very simple and rather powerful method has been developed by Zaanen et al. [39]. The most interesting feature of this approach is that, using only a few parameters (fundamental electronic energies), it has been able to account for the electronic behaviour of a great number of 3d TM oxides.

The parameters involved are (i) the d–d Coulomb interaction U (which also includes exchange), defined as the excitation energy necessary to produce charge fluctuations of the type $d_i^n \, d_j^n \gg d_i^{n-1} \, d_j^{n+1}$ (here i and j label 3d metal sites and n the 3d orbital occupation), (ii) the charge-transfer energy Δ, defined as $E \, (d_i^{n+1} \, d_j^n \, L)$-$E(\, d_i^n d_j^n)$, where L represents an anion (ligand) hole, and (iii) the ligand (W) and metal (w) one-electron bandwidths (see figure 2.9).

Thus, by comparing the corresponding values of U, Δ, W and w, TM oxides can be easily classified as insulators (Mott–Hubbard if $W < U < \Delta$ and charge transfer if $W < \Delta < U$) or metals (low U if $U < w$ and low Δ if $\Delta < W$). Since the predictions of this formalism depend (not only!) on correct values of U, Δ, W and w, it would be interesting to have a simple method to estimate them.
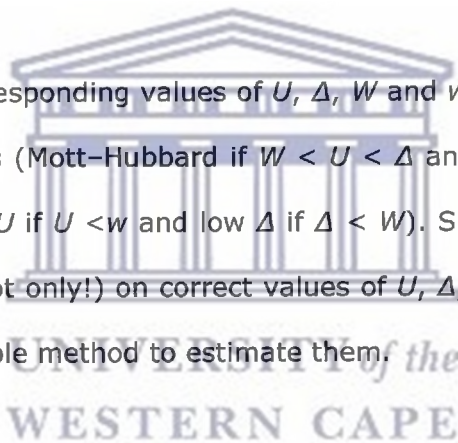
A very nice procedure has been recently developed by Torrance et al. [39] who, using only crystallographic data, gas-phase ionization potentials and Madelung energies, have been able to reproduce the electronic behaviour of a great number of oxides. The prediction of these authors for ReNiO$_3$ perovskites places these compounds not in the metallic but in the insulating region, although very close to the dividing line between charge-transfer insulators and low-Δ metals. Thus, within the framework of this simple model, the MIT transition would take place due to the opening of a charge-transfer type gap below T$_{MIT}$. This mechanism is schematically shown in figure 2.10. The narrowing of the O 2p-derived valence band is caused by the less efficient overlap of the Ni 3d and O 2p orbitals in the insulating phase.

31

In spite of the support given to the charge-transfer model by the discovery of the metal insulator transition in the nickelates with Re $\neq$ La, there is a debate concerning the mechanism responsible for the electronic localization in these compounds [40]. Thus, recently, Mizokawa *et al* [41] pointed out that, with increasing atomic number or increasing formal valence of the metal element, Δ systematically decreases. These authors stressed that Δ may become very small or negative with unusually high valences such as Fe^{4+}, Ni^{3+} or Cu^{3+}.

In this case, the d^{n+1}L configuration should be as favourable as or even more favourable than the 3d^n one. The expected charge fluctuations in the metallic state are of the type d^{n+1}Ld^{n+1}L / d^{n+1}d$^{n+1}L^2$ and the existence of a gap would be only possible in the presence of O 2p–O 2p hole correlations strong enough to split the O 2p band (p–p gap). This seems to be the case for the insulator NaCuO$_2$, where XPS measurements and the cluster calculation reported by Mizokawa *et al* [41] give a value of Δ = −2($\pm$1) eV. Following these authors, the gap in NaCuO$_2$ is neither of the Mott–Hubbard type nor of the charge-transfer type, but of the p–p type.

Like Cu in NaCuO$_2$, Ni in ReNiO$_3$ shows an unusually high (3+) formal valence. However, the existence of a p–p gap in the insulating state would require a 3d^8L (Ni^{2+} O$^-$) ground-state configuration instead of the classical assumption 3d^{7}2p^6 (Ni^{3+} O^{2-}). Even if the valence-bond calculations indicate that the latter possibility is a good starting point for an understanding of the electronic structure of these compounds [22], the absence of Ni^{3+} reported for systems as Ni$_{1-x}$Li$_x$O or La$_{2-x}$Sr$_x$Ni$_{4+\delta}$ raises severe doubts about the validity of such a crude description.

From the analysis of the x-ray absorption and photoemission spectra, a more realistic ground state, which includes the Ni–O hybridization, has been recently proposed. Thus, the relevant electronic structure of this nickelates can be
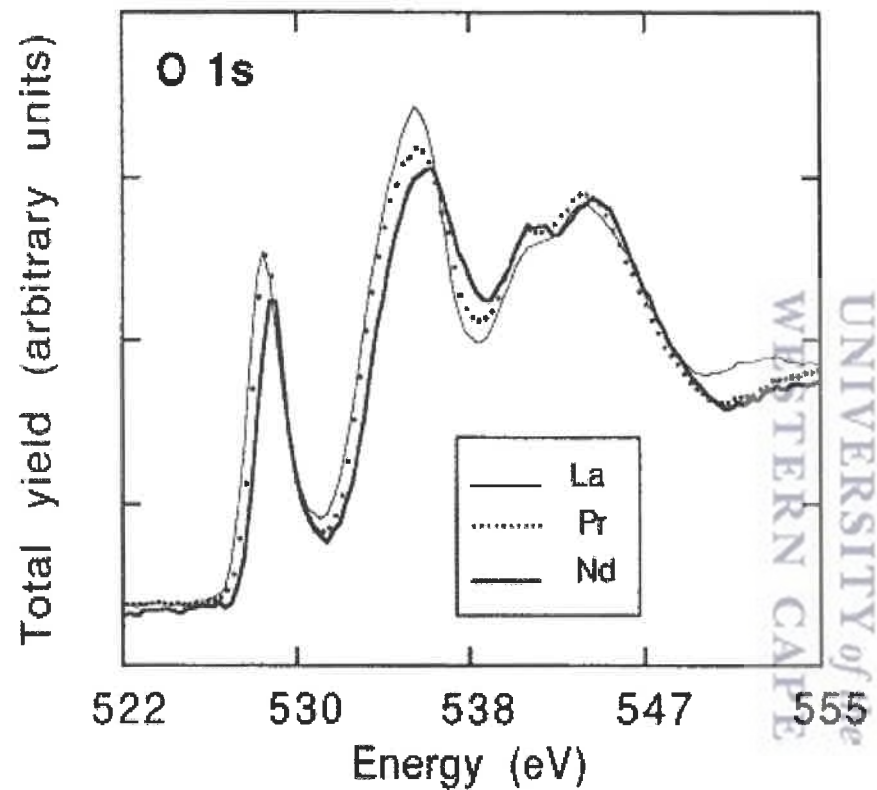
Figure 2.11

O 1s edges of LaNiO3, PrNiO₃ and NdNiO₃ at RT [40].
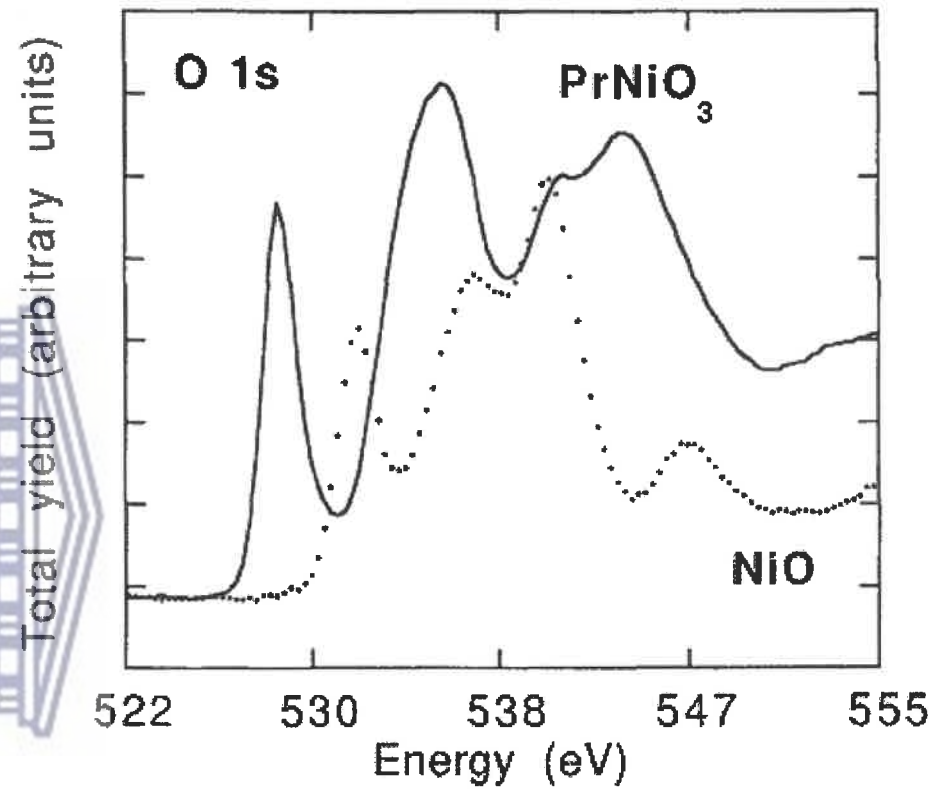
Figure 2.12

O 1s edges of PrNiO₃ and NiO at RT [40].

been extensively studied during recent years. The main features appearing in the spectra are quite similar in all the divalent compounds, and the presence of small satellites or the decrease of the multiplet splitting with smaller anion electronegativities is now well understood in terms of a covalent ground state of mainly Ni^{2+} (3d^8) character plus an anion-dependent fraction of the 3d^9L and 3d$^{10}L^2$ configurations.

For Ni^{3+} compounds, both experimental results and theoretical calculations are quite scarce. To our knowledge, the only published Ni 2p edges on compounds containing nominally trivalent Ni ions are those of PrNiO$_3$ and NdNiO$_3$ [39, 43], and the only available theoretical calculations of the Ni^{3+} 2p XAS edge have been performed by de Groot *et al* [45], considering a pure 3d^7 configuration. Intuitively, the Ni^{3+} 2p edge will show a much richer multiplet structure and higher integrated intensity than Ni^{2+} due to its extra 3d hole.

The experimental data, which show much broader structures than NiO, can in principle be interpreted as corresponding to Ni^{3+}. Unfortunately, the absence of fine structure does not allow a direct comparison with the available calculations [45]. It should be noted that, in this case, broadening is not due to the lack of experimental resolution. The quality of the NiO spectrum, obtained with the same experimental set-up, is comparable with the data obtained with the Dragon monochromator [46, 47] thus indicating that the origin of the broadening is an intrinsic property of the sample.

In order to obtain additional information about the Ni 3d–O 2p hybridization, it is very interesting to compare the ReNiO$_3$ spectra with the much more accessible Co^{2+} octahedrically coordinated experimental data [45]. Due to the atomic origin of the main features appearing in the 2p absorption edges of 3d transition metals, we expect strong similarities between Co^{2+} and Ni^{3+} spectra due to their common
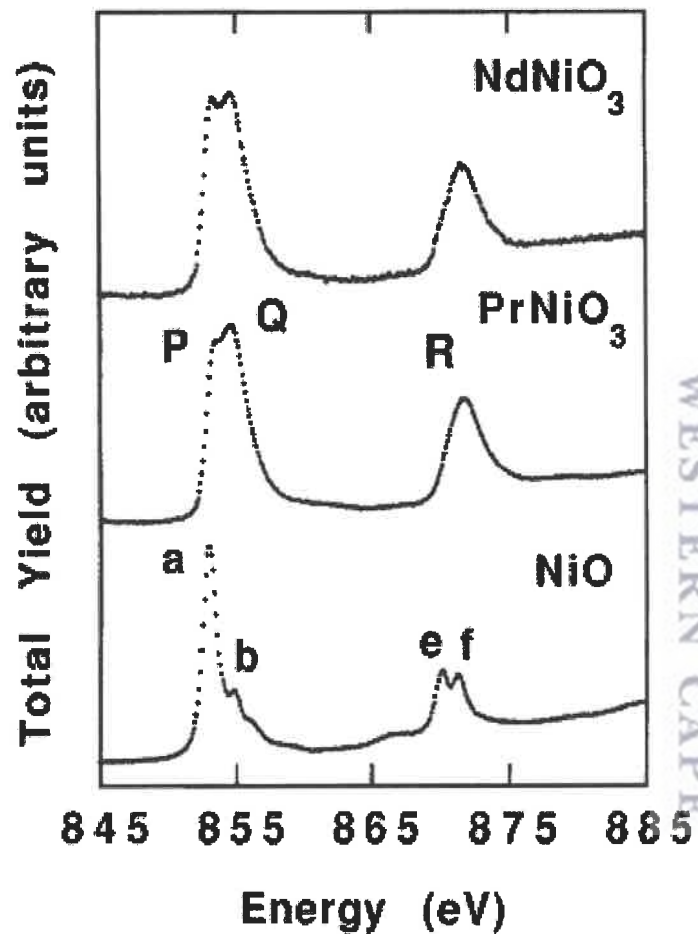
Figure 2.13

Ni 2p edges of NiO, PrNiO₃ and NdNiO₃ at RT [39].
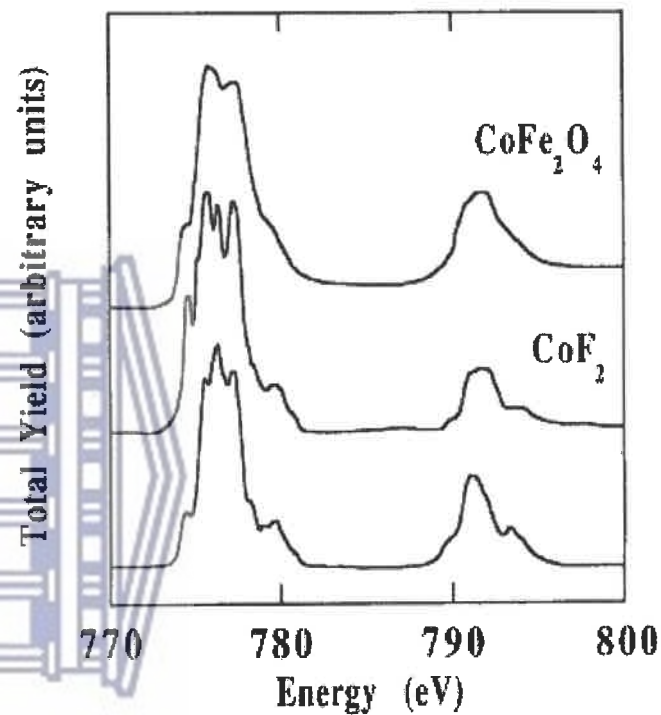
Figure 2.14

Co 2p edges of CoFe2O₄ and CoF₂. Bottom, a theoretical calculation of the Co 2p edge [39].

39

decrease in size of the lanthanide ions. The relevant parameter controlling the metal–insulator transition temperature as well as the stability of the different crystallographic structures found along the series is the Ni–O–Ni superexchange angle θ. The increasing overlap between the O 2p and Ni 3d orbitals which occurs on moving from Lu (ra = 0.977 Å) to La (ra = 1.160 Å) favours the metallic state (T_{MIT} decreases) as well as the AF state (T_N increases).

The collapse of both tendencies occurs for ra =1.10 Å, T_N being identical to T_{MIT} for the nickelates with larger ionic radius (NdNiO$_3$ and PrNiO$_3$). This behaviour is illustrated in figure 2.15, where the evolution of T_{MIT}, T_N and the orthorhombic-rhombohedral transition temperature T_{R-O} as a function of ra has been displayed.

The results of the different techniques reviewed along this chapter give some elements for the understanding of the mechanism responsible for the T_{MIT} transition in the nickelates. The most important points to be retained are the following:

(i) The change in the transport properties at T_{MIT} is abrupt.

(ii) The associated structural changes are also discontinuous although very small.

(iii) A rather unusual 3D antiferromagnetic order develops in the insulating state, which, within the framework of the current theories about superexchange in oxides, can be only explained by supposing the existence of an orbital superlattice.

The three kinds of effect (structural, electronic and magnetic (not developed on this present work)) which coexist at T_{MIT} (at least for PrNiO$_3$ and NdNiO$_3$) suggest several possibilities for the driving mechanism of the gap opening. A magnetic origin, which was at the beginning one of the most exciting possibilities, has been recently disregarded after the observation in SmNiO$_3$ ($T_N \neq T_{MIT}$) of the same magnetic structure as in the nickelates with $T_{MIT} = T_N$.

To definitively reject this possibility, it would be however necessary to verify whether, as in the case of high-Tc superconductors, magnetic correlations are still present in the $T_N < T < T_{MIT}$ range.

Concerning the possibility of a Jahn–Teller distortion, high-intensity neutron diffraction experiments show that, if they exist, the superstructure peaks associated with the orbital ordering are at least 104 times smaller than the main nuclear peaks. Thus, within the present experimental accuracy, the structural changes below MIT simply consist of an enhancement of the orthorhombic distortion existing at higher temperatures. Single crystals and/or high-intensity synchrotron measurements would be necessary to decide about the existence of an additional structural distortion concomitant with the T_{MIT}.

Considering pure (not magnetic) electronic correlation, three kinds of gap are likely to occur: Mott–Hubbard type, charge-transfer type and negative-Δ type. The first estimation of Δ and U reported by Torrance et al. [8] for LaNiO$_3$ gave $U-\Delta \approx 5$ eV, that is, they suggested the opening of a charge transfer gap below T_{MIT}.

The experimental verification of the hypothesis, which has since remained the consensus view, is however not straightforward. Though some x-ray spectroscopic measurements are actually available, their analysis is far from trivial and depends strongly on the particular technique used.

In summary, the nature of the mechanism responsible for the MIT in ReNiO$_3$ perovskites is still an open question. Though some 'key' experiments (most of them rather difficult to realize) would help to decide between the different possibilities, one of the major limitations to advance in our current understanding is the limited scope of the actual theories. More sophisticated mechanisms going

[16] Zaicheng Sun, Dong Ha Kim, Markus Wolkenhauer, Gabriela Gina Bumbu, Wolfgang Knoll, and Jochen S Gutmann ChemPhysChem 7, pp370-378, 2006

[17] Landolt–Bornstein, New Series 1970 Group III, vol 4a, ed K H Hellwege and A M Hellwege (Berlin: Springer) ch 3, p 126.

[18] Goldschmith V M 1926 Skr. Nor. Vidensk. Akad. Mat. Naturvidensk. Kl. 2 1

[19] Wold A, Post B and Banks E 1957 J. Am. Chem. Soc. 79 4911

[20] Geller S 1956 J. Chem. Phys. 24 1236

[21] Bertaut E and Forrat F 1956 J. Physique Radium 17 129

[22] Garcia-Mu~noz J L, Rodrıguez-Carvajal J, Lacorre P and Torrance J B 1992 Phys. Rev. B 46 4414

[23] Medarde M, Rosenkranz S and Lacorre P in preparation

[24] Poix P 1970 C. R. Acad. Sci., Paris 270 1852

[25] Rodrıguez-Carvajal J, Rosenkranz S, Medarde M, Lacorre P and Trounov V 1997 Phys. Rev. B submitted

[26] Medarde M, Garcia-Munoz J L, Rosenkranz S, Lacorre P and Fischer P 994 Physica B 194–196 367

[27] Granados X, Fontcuberta J, Obradors X and Torrance J B 1992 Phys. Rev. B 46 15 683

[28] Granados X, Fontcuberta J, Obradors X, Ma~nosa J L and Torrance J B 1993 Phys. Rev. B 48 11 666

[29] Katsufuji T, Okimoto Y, Arima T and Yokura Y 1995 Phys. Rev. B 51 4830

[30] Medarde M, Purdie D, Grioni M, Hengsberger M, Baer Y and Lacorre P 1997 Europhys. Lett.

[31] Eisaki H, Uchida S, Mizokawa T, Namatame H, Fujimori A, van Elp J , Kuiper P, Sawatzky G A, Hosoya S and Katayama-Yoshida H 1992 Phys. Rev. B 45 12 513

[32] Ashcroft N W and Mermin N D 1988 Solid State Physics (Tokyo: Holt-Saunders) ch 1, p 5

[48]   Garcia J, Blasco J and Proietti M G 1995 Phys. Rev. B 52 15 823

[49]   Barman S R, Chainani A and Sarma D D 1994 Phys. Rev. B 49 8475.

UNIVERSITY *of the*

WESTERN CAPE

Due to the correlation between these physical mechanisms involved in PLD process, only an approximated description of the phenomenon is possible. This is the reason why it does not exist a theoretical model describing the whole PLD process. Instead, there exist several models, each of them analyzing in detail only one aspect of it, as the vaporization [5], the plasma formation [6], [7] and its expansion in vacuum [8], [9] or in presence of an ambient gas [10], [11].

In particular, plasma expansion dynamic, that plays a crucial role in pulsed laser deposition, is not yet totally understood, even in the simpler case of propagation in vacuum. Furthermore, the expansion behavior is even more complex in presence of an environmental gas, often used during PLD deposition of complex oxides. In such case, additional physical processes affect the plume expansion behavior, such as plume deceleration and splitting, shock-wave formation, thermalization, etc. [12], [13], [14] as a consequence of plasma–background gas interaction.

In this section, the main aspects of the PLD process are described, from the initial laser-target interaction, up to the film nucleation and growth, when the plume reaches the substrate. In particular, the attention will be focused on the plasma expansion dynamic and plasma substrate interaction reporting some models widely used for describing this process in vacuum and in presence of ambient gas.

3.1 Laser ablation mechanisms

In the pulsed-laser deposition (PLD) method, high power laser pulses are used to evaporate material from a target surface such that the stoichiometry of the material is preserved in the interaction. At the early stage of the laser pulse a dense layer of vapour is formed in front of the target. Energy absorption during the remainder of the laser pulse causes, both, pressure and temperature of this vapour to increase, resulting in partial ionization.

49

exact description of the phenomenon. For this reason it is widely used a macroscopic approach, based upon an energetic balance: the problem is transformed in the calculus of the temperature distribution on the sample, after the interaction with laser radiation. The target region interested by the ablation process has the xy sizes of the laser spot dimension on target surface, times an L_{th} dimension, on the z direction perpendicular to the target. Such value of L_{th} depends on the thermal diffusivity of the sample material and on the pulse duration as $L_{th} = \sqrt{2D\tau_L}$ where D is the thermal diffusivity and τ_L is the pulse duration [15], [16], [17]. It can be seen, the longer the pulse, the deeper and the wider is the laser affected zone.

Since the value of L_{th} is usually very much smaller than the laser beam irradiated zone on the target surface, one can assume that the thermal gradient in the transverse plane xy of the target face is irrelevant with respect to the thermal gradient in z direction normal to the target. In this approximation, the temperature distribution T(r, t) into the irradiated target is given by the one dimensional heat equation [15], [18], [19].
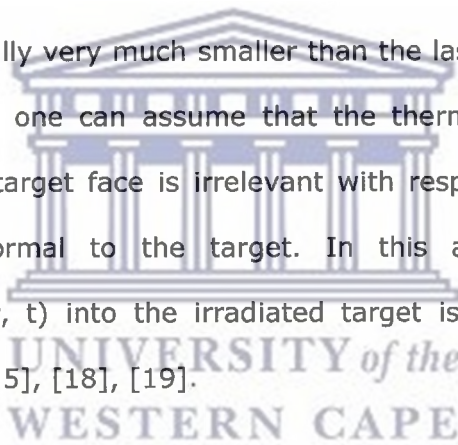
In general the interaction between the laser radiation and the solid material takes place through the absorption of photons by electrons of the atomic system. The absorbed energy causes electrons to be in excited states with high energy and as a result heat the material up to very high temperatures in a very short time. Then, the electron subsystem will transfer the energy to the lattice, by means of electron-phonon coupling.

In this frame, the temporal and spatial evolution of the electrons subsystem and the lattice should be described by means of two different temperatures: T_e (electrons) and T_i (lattice), on the base of the two temperature diffusion model,

3.4 Plasma plume expansion

Since the onset of the material removal described in the previous sections takes place within a very short time after the pulse (1-100 ps), on the time scale of the plasma expansion (μs) the laser–target event can be regarded as a momentary release of energy. The spatial structure of the vapour plasma at the early stage of its expansion is well known to be a cloud strongly forwarded in the direction normal to the ablated target. The reason of this characteristic plasma elliptic shape, called plume, is in the strong difference in pressure gradients in axial and radial directions: the plasma expands in the direction of maximum pressure gradient.

Among the several models dealing with plume expansion, a first distinction should be done between plume expansion in vacuum and in an environmental gas. In the following, some approaches to the description of the plume expansion in a vacuum as well as into a background atmosphere will be briefly illustrated.

In vacuum, the plasma will expand in a way similar to a supersonic expansion with a free linear behaviour and a weak fluorescence will be visible, close to the target, due to collisions between the plasma species occurring just after the termination of the laser pulse. The plume expansion dynamic in vacuum was extensively investigated by Anisimov et al. [8] and by Singh and Narayan [9], resorting to a self-similar expansion of an elliptical, neutral gas cloud.

The two previous cited models differ essentially for the analysis of the plume expansion during the first stage, which timescale is of the order of the laser pulse duration. Then, after the laser pulse, both models hypothesize an adiabatically expanding plume, in which the plume energy, initially purely thermal, is progressively transformed into kinetic energy during the expansion. After a short

measurements, showing a initial plume front velocity value very close to that observed in a vacuum (10^6 cm s^{-1}) [26], [8], [27].

During the plume expansion, the gas adjoint mass on the plume front increases. The mass of the plume and the adjoint background mass swept away during the propagation, are considered confined into a hemispherical thin layer at the plume front. The Predtechensky et al. and the Arnold et al. models differ in their basic hypothesis and physical assumption.

The approach used in the Predtechensky and Mayorov model describes the dynamics of the front expansion of a plume into a background gas considering a hemispherical plume expansion, as schematically shown in figure 3.1. This model considers the balance between the linear momentum Q of the total mass (i.e. plume and adjoint background gas) confined into an infinitely thin layer at a distance R from the centre O and the force F acting at the periphery of the hemispherical thin layer due to the background gas pressure p_0. Here the boundary of the plasma plume R_i, of the external shock wave R_e and of the contact front R are equal, i.e. $R_i = R_e = R$.

The progressive increase of the background mass at the plume periphery leads to a gradual reduction of the plume front expansion velocity, until a stopping stage is finally reached. Even using a simple physical approach, which does describe the basic influence of the background gas on the plume dynamics, the model allows its applications in different cases without requiring complex numerical methods and calculations.

Contrary to Predtechensky and Mayorov model, Arnold et al. [10] developed a more complete model, which takes into account also the processes involved in plume-background gas interaction affecting to the plume internal structure. In

55

Ambient atmosphere

External SW

Internal SW

Contact front

Ablated target
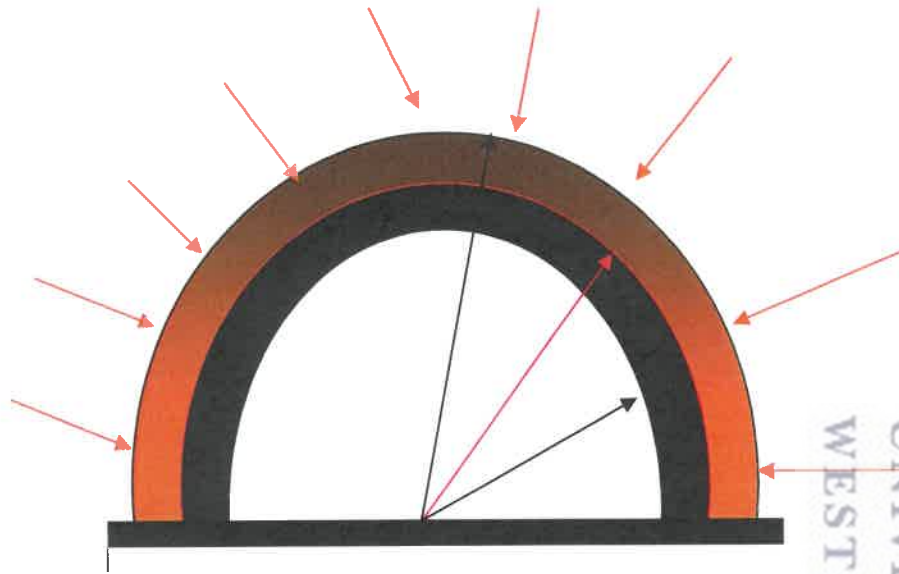
Figure 3.1

Sketch of the Predtechensky and Mayorov plume gas interaction model: The boundary of the plasma plume R_i, of the external shock wave R_e and of the contact front R are shown.
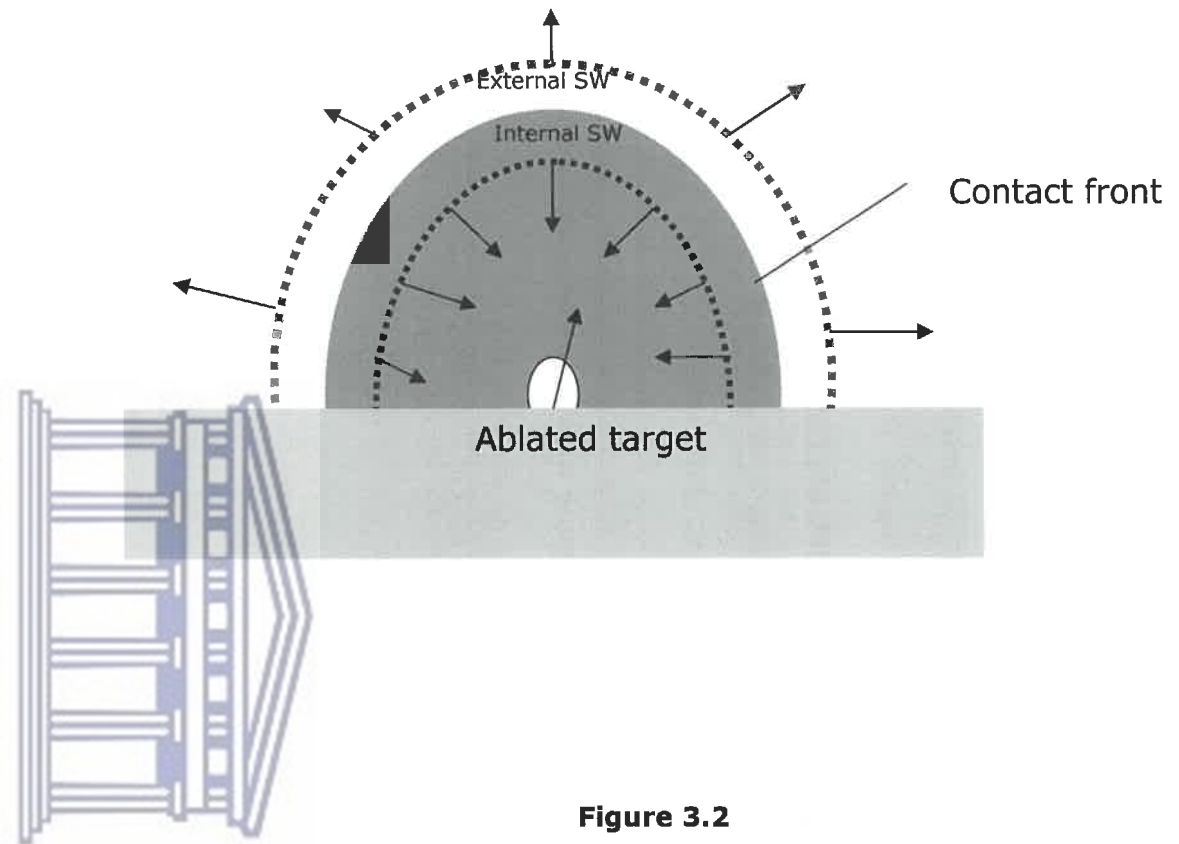
Figure 3.2

A scheme of the plume in the Arnold et al. expansion model. R_0 is the initial radius of the plume. The contact front between the plume and the ambient (R_c) is moving with the velocity R'_c. (R_{SW}) denotes the front of the external shock wave propagating in ambient gas. The internal shock wave (R_i) propagates inwards, to the center of the plume.

The raise of the background pressure generally leads to the following effects that depart from the free expansion behaviour:

- an increase of the collisions on the expansion front with an increase of the fluorescence coming from all the species;
- a sharpening of the plasma boundary that indicates the presence of a shock wave front;
- a spatial confinement of the plasma due to a decrease of its velocity, determined by the repeated collisions with the gas molecules.

The plasma expansion in a gas environment has been also described in the literature in terms of different phenomenological models depending on the experimental regimes, affected by the pressure range of the gas present during the deposition process, by the energy of the plasma species and by the temporal stage of propagation [30, 31, 32]. At low pressure and in the early times of the expansion, the plasma dynamics is in good agreement with the drag-force model [33]. In this model the ejected species are regarded as an ensemble that experiences a viscous force proportional to its velocity V through the background gas $V = V_0 e^{-\beta t}$ or analogously $R = R_0 \left(1 - e^{-\beta t}\right)$ where R indicates the position of the front edge of the plasma, R_0 the distance at which the plasma propagation ceases (it is generally indicated as the stopping distance) and β a slowing coefficient. Both R_0 and β are phenomenological parameters whose values are, necessarily, determined by fitting the experimental data.

As reported in some works [33, 34], the estimated R_0 values are more than one order of magnitude larger than the calculated inelastic mean free path λ values. Such large differences are presumably due to the fact that R_0 is a rather complex function of several experimental parameters such as the background gas nature

geometrical and thermodynamic quantities, E is the plasma energy and ρ_0 the density of the undisturbed gas.

This model can strictly be applied only when the mass of the gas surrounding the shock wave is higher than the mass of the ablated material and only up to distances from the target at which the pressure driving the moving front of the plasma is greater than the pressure of the gas at rest. Then the shock wave can be observed only in a limited spatial region given $\left(\dfrac{3M_0}{4\pi\rho_0}\right)^{1/3} << R << \left(\dfrac{E}{P_0}\right)^{1/3}$ where M_0 is the mass of the expanding plasma and P_0 is the pressure ahead of the shock wavefront [32, 33].

In the shocked region, the temperature raises reaching values of the order of several thousand of Kelvin degrees and producing an enhancement of the optical emission from the excited species in the plasma. The temperature values in this region can be obtained starting from the equation of state for a polytropic gas [37] given by $T_S = \dfrac{2\gamma}{\gamma+1}\left[\dfrac{\gamma-1}{\gamma+1}M^2+1\right]T_0$ where γ is the specific heats ratio (≈ 1.2), M the Mach number and T_0 the temperature of the undisturbed gas.

The Mach number can be evaluated from the V=R/t data, where M=V/υ_s, R indicates the position of the shock wave moving front, and υ_s is the sound velocity. In the same way it is possible to obtain the relation for the shocked region density ρ_S from the relation $\rho_S = \rho_0\,\dfrac{\gamma+1}{\gamma-1}$.

In this region, the reached temperature values can influence the physical and chemical behaviors of the species. In reality, the chemical reactions can take place only if a sufficient mixing between the plasma and the gas species occurs. Such a mixing is governed by the diffusion processes across the contact surface

temporally unified so that a single analytical curve gives a complete description of the phenomenon.

Experimentally, the chemical nature of the background gas, its pressure and the plasma energy can determine the occurrence of one or more of these regimes and a family of R-t curves can be obtained. If these R-t experimental data are expressed in terms of the following dimensionless variables:

$$\tilde{R} = R\left(\frac{2E}{P_0}\right)^{-1/3} \quad ; \quad \tilde{t} = t\vartheta_S\left(\frac{2E}{P_0}\right)^{-1/3}$$ where υ_s is the sound velocity in the ambient

gas, P_0 is the known pressure of the gas and E is the total energy of the plasma, then all of points will fall into a single curve. The energy of the plasma E depends on the coupling between the laser pulse and the target material and it is just a fraction of the laser energy.

In this work we adopt this latest approach to explain our results: we express all experimental data in dimensionless variables according to Arnold et al. [38] model. Depending on the adopted experimental conditions all of the three stages, free expansion (R ∞ t), shock can be formation (R ∞ $t^{2\backslash5}$) and the onset of the plume stopping were observed. Estimates of the plasma energy values can be also obtained from dimensionless variables applied to the R-t data in a limited range, i.e. where the ideal shock wave behaviour can be observed.

3.5 Plume-substrate interaction

In PLD, the deposition of the ablated material on the substrate surface can be regarded as instantaneous for every pulse, since the time scale of the atomistic processes involved in the film growth exceeds the deposition pulse duration.

Each instantaneous deposition is followed by a relative long time interval, where no deposition takes place. Because of the instantaneous deposition at typical PLD

63

In the following a schematization of the possible ways of growth, determined by the thermodynamic approach of the balance between the free energies of film (γ_F) and substrate (γ_S) and the interface between film and substrate (γ_I) is given.

When the total free energy of the film surface and the interface equals the free energy of the substrate surface ($\gamma_F + \gamma_I < \gamma_S$), significant wetting is expected. This leads to layer-by-layer growth as described by Frank and Van der Merwe [41].

In the case of an increased total free energy wetting is energetically unfavorable and the deposit will take place minimizing the film substrate interface by means of islands growth; this is the case of Volmer-Weber mechanism [42], where the energy due to the creation of interface is higher than the surface energy of the substrate and film ($\gamma_F + \gamma_I > \gamma_S$).

At the intermediate case, a transition from the Frank and Van der Merwe to the Volmer-Weber growth mode can be observed. Here a crucial role is played by the mismatch between film and substrate, inducing a strain on the growing film. A layer-by-layer growth takes place in the first stage. Then, the thicker become the film, the higher is the elastic energy due to the strain. Such large strain energy can be lowered by forming islands in which strain is relaxed. This mechanism results in a continuous film of one or two monolayers onto which successively discrete islands are formed. This way of growth is the so-called Stranski-Krastanov [43].

In the Figure 3.3, the previous regimes are depicted. The previous approach doesn't take into account the effect on the growth kinetic of the deposition parameters, such as the value of supersaturation in the gas phase, the substrate vicinality and the crystallographic misfit between the film and substrate unit cells.

65

In heteroepitaxy, the misfit usually induces Volmer-Weber growth, except for large interface energies between substrate and deposited film, which cause the Stranski-Krastanov growth. The substrate vicinality provides terrace surface, separated by steps. The steps heights and the terraces length depend on the angle and the direction of the miscut. On a vicinal substrate, beside the growth modes described above, a fourth way of growth can occur: the step-flow mode (see panel (b) in Figure 3.3).

This growth mode takes place on vicinal surface with high steps density and small terraces, in some deposition condition. In this case, the steps act as a sink: the adatoms diffuse towards the substrate steps preventing the nucleation on the terraces. As result, steps will propagate during the growth.

Since the diffusing adatoms attach to the step edges, the result is the advancement of the steps of the substrate surface. This growing mode will go on indefinitely, with no changes in the starting substrate surface morphology, if both the terraces will keep the same width and the step ledges remain straight.

Otherwise, step bunching can occur: in this case a high density of steps moves with large velocities over the growth surface. By fluctuation, higher steps catch up with lower ones and then move together as double, triple steps. Subsequently, the distribution in the terrace length (l_T) broadens [40].

3.7 Growth kinetics

For the sake of simplicity, in the following it will be discussed the growth kinetics in the homoepitaxy case, where complicating effects as lattice parameter misfit and thermal coefficient expansion do not play a role.

Once adsorbed on the surface an atom, now called adatom, may desorb into the vapor or change adsorption site, in which case it can diffuse on the surface for several atomic length, before to be detached and incorporated in the crystal structure, as schematized in Figure 3.5.

The molecule-surface interaction is described by a potential that is a periodic function of the two coordinates parallel to the surface and a decreasing function of a third coordinate normal to it. If L_T is the terrace length, we define L_D as the average distance an atom can travel on a flat surface before being trapped. It is given by $L_D = \sqrt{D_S \tau}$ where (D_s) is the surface diffusion coefficient of the adatoms, and τ is the residence time before re-evaporation.

The surface diffusion coefficient D_S is generally expressed as $D_S = a^2 \upsilon \exp\left(-\dfrac{E_A}{k_B T}\right)$ where E_A is the activation energy for diffusion, a is the characteristic jump distance and υ is the sticking coefficient.

The sticking coefficient expresses the probability of a molecule to be captured, once impacting on the substrate surface and it is given by the ratio of the captured molecules to the total number of molecule hitting the surface.

In this case the interlayer mass transport plays a big role to determine the growth mode. In fact, to obtain a layer-by-layer growth mode in this situation, a steady interlayer mass transport should be present so that atoms deposited on top of a growing island must reach the island edge and then diffuse to a lower layer.

In the ideal case, the nucleation starts after completion of a layer. But if there is no interlayer mass transport, nucleation will occur on top of islands before these have coalesced and this is the case of the so called second layer nucleation. The probability for second layer nucleation is related to the mean island radius at the time of stable clusters nucleation on top of the islands, R_C.

The value of R_C is, in turn, related to the parameter E_S, that is the energy barrier for an atom to descend across the step edge to a lower terrace. Larger is the value of E_S, smaller will be the value of R_C, since the additional energy barrier lead to accumulation of the adatoms on top of the islands, with subsequently increase of second layer nucleation rate. In the real system the growth mode is in between these growth modes described here.

In some cases, even a transition from a layer-by-layer to a step flow growth on vicinal substrate can happen when the diffusion length of adatoms becomes comparable to the terrace width, i.e. when $L_D \approx L_T$.

This can happen because either the substrate temperature, determining the surface diffusion length L_D or the vicinal angle, determining the terrace width L_T, is changed.

3.8 Advantage of the PLD

The main advantages of PLD are its ability to create high-energy source particles, permitting high quality film growth at low substrate temperatures, typically ranging from Room temperature to 800 °C, its simple experimental setup, and operation in high ambient gas pressures in the range 10^{-5}–10^{-1} Torr.

The PLD technique allows preparing all kinds of oxides, nitrides, carbides, but also polymers, Buckminster fullerenes or metallic systems. In order to obtain all these different kinds of materials, one has to work in ultrahigh vacuum (UHV) or reactive gas atmosphere during deposition. This is possible with PLD, because the energy source is outside the deposition chamber. During growth of oxides, the use of oxygen is often inevitable for achieving a sufficient amount of oxygen in the growing oxide film. For instance, for the formation of perovskite structures at high substrate temperatures in a one-step process, an oxygen pressure of about 0.3 mbar is necessary [44]. Also, for many other oxide or nitride films, the necessity of working in a reactive environment makes it difficult to prepare such samples vice thermal evaporation, using electron guns. In the case of sputtering, where commonly argon is used as the background gas, a larger amount of oxygen or nitrogen can only be added in special oven facilities close to the substrate surface.

The PLD technique is also flexible, because the spot size of the focused laser beam is small and, therefore, the target area may even be less than 1 cm^2. This allows preparing complex samples with enrichments of isotopes or isotopic markers within the deposited film. Being able to easily prepare samples for research purposes or for application tests is especially interesting, if the sample or one component is extremely expensive or impossible to prepare with other

73

3.9 Conclusion

The PLD technique is based on the ablation process of a material induced by focusing a high energy pulsed laser on its surface. In spite of the simplicity of the experimental setup, the physical phenomena involved in the ablation process are very complex. The involved mechanisms depend on the optical and structural properties of the target material and on the characteristics of the incident radiation such as the wavelength and the energy density. The stream of atoms, molecules and clusters that is ejected from the target surface during the ablation process, commonly known as "plume", rapidly expands, in vacuum or through a gas, towards the substrate surface. Although a lot of experimental and theoretical work has been done, many effects of the interaction of the laser beam with different targets in an ambient atmosphere are still not satisfactorily explained. It is known that, being the plume composed of excited neutral and ionized species, it emits radiation that can be appropriately analyzed to obtain information about its composition and dynamics.

In particular, by means of fast photography measurements, different regimes of the laser induced plasma expansion dynamics have been evidenced. This information can be strictly correlated with the structural properties of the deposited thin films and can so give a very useful contribution to the comprehension and to the control of the deposition process itself.

In this work, in addition of the ICCD fast photography to study the plasma dynamic, the properties of the deposited films will be characterized by means of XRD, RBS, Four points probe, SEM, AFM and Raman spectroscopy.

The details of the instrumentations and of the experimental techniques are described in the following chapter.

[18]   J.F.Ready, Effects of High-Power Laser Radiation, Academy Press, New York (1971)

[19]   A.Peterlongo, A. Miotello, R.Kelly Phys. Rev. E 50, 4716 (1994)

[20]   S.I.Anisimov,B.S.Luk'yanchuk Physics 45, 293-324 (2002)

[21]   M.I.Kaganov, I.M.Lifshitz, L.V. Tanatarov, Sov.Phys JEPT 4, 173 (1957)

[22]   B. N. Chichkov, C. Momma, S. Nolte, F. von Alvensleben, and A. Tnnermann, Appl.Phys. A 63, 109 (1996)

[23]   S. Nolte, C. Momma, H. Jacobs, A. Tnnermann, B. N. Chichkov, B.Wellegehausen, and H. Welling, J. Opt. Soc. Am. B 14, 2716 (1997)

[24]   Ya.BZel'dovic, Yu.P.Raizer, Physics of shock waves and high temperature hydrodinamic phenomena Academic Press, New York, (1966)

[25]   R.W. Dreyfus, Appl.Surf.Sci 283, 177 (1993)

[26]   S.Amoruso, A.Sambri, X.Wang J.Appl. Phys. 100, 013302 (2006)

[27]   P.E.Dyer A.Issa, P.H.Key App.Phys.Lett. 57, (1990)

[28]   Singh R.K., Holland O.W., Narayan J., J. Appl. Phys. 68 233 (1990)

[29]   S.Amoruso, B.Toffman, J.Schou Phys. Rev. E 69, 05643 (2004)

[30]   H.J. Dang, M.F. Zhou, Q.Z. Qin, Appl. Surf. Sci. 140, 118 (1999).

[31]   M. Okhoshi, T. Yoshitake, K. Tsushima, Appl. Phys. Lett. 64, 3340 (1994).

[32]   W.K.A. Kumuduni, Y. Nakayama, Y. Nakata, T. Okada, M. Maeda, J. Appl. Phys. 74, 3340 (1993).

[33]   D.B. Chrisey, G.K. Hubler, D. Geoheagan, Pulsed Laser Deposition of Thin Films (Wiley, New York 1994) Chap.5.

[34]   J. Gonzalo, C.N. Afonso, I. Madariaga, J. Appl. Phys. 81 951 (1997).

[35]   P.E. Dyer, A. Issa, P.H. Key, Appl. Phys. Lett. 57, 186 (1990).

[36]   Y.B. Zel'dowich, Y.P. Raizer,Physics of Shock Waves and High Temperature Hydrodynamic Phenomena(Academic Press, New York 1966).

[37]   L.D. Landau, E.M. Lifhitz, Fluid Mechanics, 2nd edn.(Pergamon Press, Oxford 1987).

[38]   N. Arnold, J. Gruber, J. Heitz, Appl. Phys. A 69, S87 (1999).

CHAPTER IV

4. Experimental Set-up

To date many techniques have been used for growing $ReNiO_3$ nickelate compounds thin films. The difficulty of preparing these compounds in the series of $ReNiO_3$ increases severely as the radius of the rare earth decreases. Generally, it requires oxides reaction above 1000°C under excessive oxygen pressures of about 200 bars during several days. It is therefore intended within this project to exploit the high temperature-high induced shock wave pressure of the laser ablation phenomenon.

In this chapter, a detailed description of the experimental work performed to deposited nanostructured thin films of $Sm_{0.55}Nd_{0.45}NiO_3$ solid solution system by pulsed laser deposition is presented. The principles and experimental conditions of the different characterization techniques used are successively also reviewed and discussed.
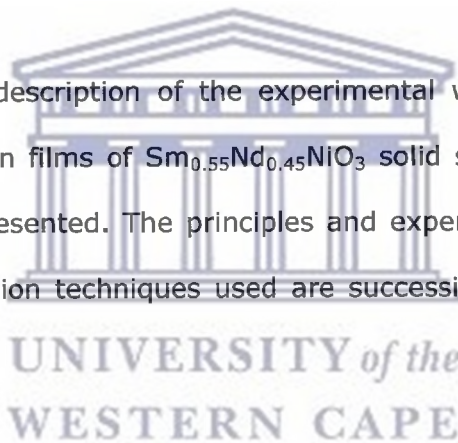
4.1 PLD chamber

4.1.1 Targets preparation

Concerning the targets preparation technique employed, the targets were synthesized from a mixture of simple oxides. The targets were prepared from stoichiometric amounts of simple oxides, i.e. Nd_2O_3 (Aesar 99.9%), Sm_2O_3 (Aesar 99.9%), and NiO (Aesar 99.9985%). To ensure stoichiometry, the first two oxides were heated at 900 °C overnight to remove any absorbed water, and all weighting was performed in an atmosphere of ultra high-purity argon.

For each sample, an amount of NiO was weighed first, and amounts of the other oxides were weighted to within 0.02% of the values calculated from the weight of

Figure 4.1

Schematic photograph of the stainless-steel die used to make
the pellet.

81
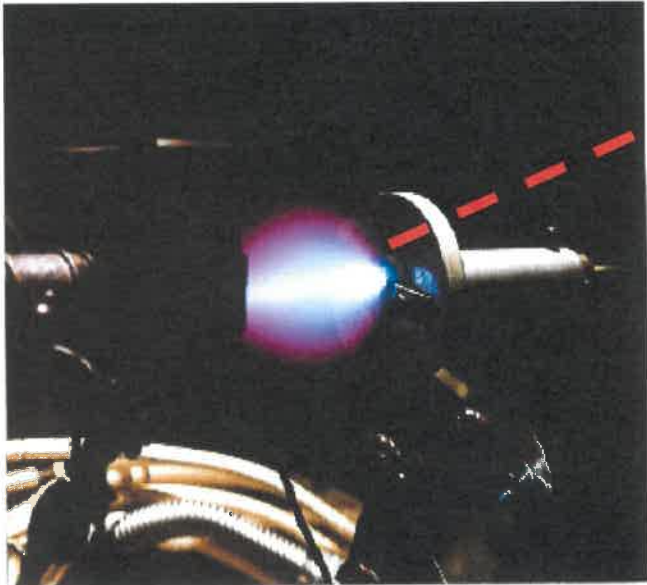
Figure 4.2

Photograph image of the PLD system used for the synthesis of the samples

83

4.2 Films Characterization techniques

4.2.1 Rutherford Backscattering (R.B.S)

Rutherford backscattering Spectrometry (RBS) provides a simple, fast and direct method to obtain elemental depth profiles in solid. In a RBS experiment light ions low energies, usually in the range 1-3 Mev, are scattered on solids to be investigated. At these energies only elastic collisions occur, and these way nuclear reactions are avoided.

A mono-energetic ion beam (H^+, He^+ or He^{++} is directed onto the sample, and then a solid state detector is used to analyze the elastically backscattered particles. Samples are placed in Vacuum ($\approx 10^{-6}$ kPa) while being analyzed. The sample normal is usually tilted 10 degrees with respect to the ion beam, and only those particles backscattered at 165 degrees are analyzed by the detector. A permanent horseshoe magnet is used to prevent secondary electons from escaping from the target.

Rutherford backscattering spectrometry relies on three concepts for an analytical capability of the method:

- The kinetic factor (mass analysis);
- The differential scattering cross-section (quantitative analysis);
- The energy loss of a particle (depth analysis).

In the laboratory system of coordinates the energy of the particle is determined by its own mass m, the mass M of the target atom and the scattering angle θ. The typical geometry for backscattering is shown below in figure 4.3. After the consideration of the conservation of momentum and kinetic energy the kinematic factor is defined as the ratio of the projectile energies after (E_1) and before (E_O) collision as,
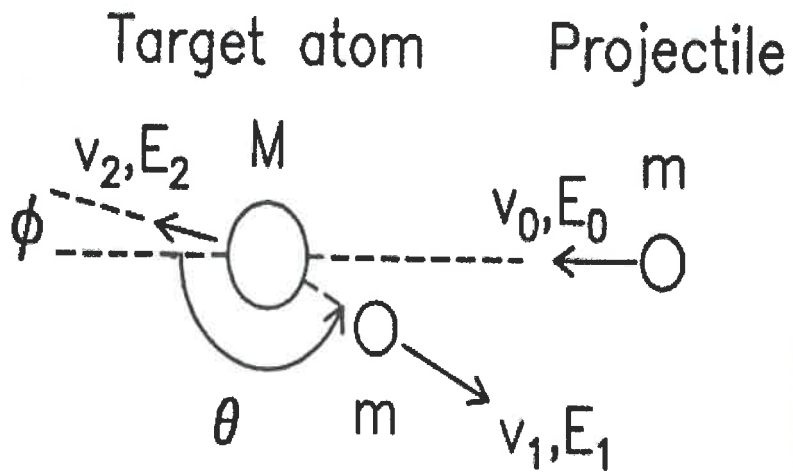
Figure 4.3

Geometric representation of elastic scattering of the projectile atom,mass m, from a target atom, mass M during RBS.

Figure 4.4

Van de Graaf acquisition data system during RBS of MRG at iThemba LABS.

87

The total energy loss of the changed particle in the compound $A_m B_n$ can thus be

given as $\Delta E = [s]^{A_m B_n} t = \dfrac{m}{m+n}[s]_A^{A_m B_n} t + \dfrac{n}{m+n}[s]_B^{A_m B_n} t$. The height of the spectrum

H gives the number of backscattered particles with energy in certain energy

internal δE. Between E and δE is given by $H = n_0 \Omega \left(\dfrac{d\theta}{d\Omega}\right) N \dfrac{\delta\theta}{[s]} \dfrac{1}{\cos\theta_1}$ where n_0

is the number of incident particles, Ω the solid angle of the detecting system and

N the atomic density, while $\dfrac{d\theta}{d\Omega}$ and [s] are given by the expansion on the top.

The height of the spectrum H_A for element A in the compound $A_m B_n$ can be given

in the same way as equation $H = n_0 \Omega \left(\dfrac{d\theta}{d\Omega}\right) N \dfrac{\delta\theta}{[s]} \dfrac{1}{\cos\theta_1}$.

$H_A = n_0 \Omega \left(\dfrac{d\theta}{d\Omega}\right)_A N_A \dfrac{\delta\theta}{[s]} \dfrac{1}{\cos\theta_1}$ Where N_A refers to the density of element A in the

$A_m B_n$. $H = n_0 \Omega \left(\dfrac{d\theta}{d\Omega}\right) N \dfrac{\delta\theta}{[s]} \dfrac{1}{\cos\theta_1}$ a similar equation holds for H_B the height of

spectrum peak for element B. it is obvious that N_A and N_B are proportional to m

and n, thus $\dfrac{H_A}{H_B} = \dfrac{\sigma_A}{\sigma_B} \dfrac{m}{n} \dfrac{[s]_B^{A_m B_n}}{[s]_A^{A_m B_n}}$

4.2.2 X-Ray Diffraction Technique

X-Ray Diffraction technique has been extensively used to determine the

crystallographic information, analysis of the elemental composition of thin films as

well as to uniquely identify crystalline phases near solid surface. This technique

is most suited to films of thickness greater than a few ten nanometers.

The X-ray diffraction methods have qualitative and quantitative analysis.

Qualitative analysis involves the identification of phase or phases in a specimen

by comparison with the reference pattern (i.e. data collected by someone else),

is characteristic of the sample. Where a mixture of different phases is present, the resultant diffractogram is formed by addition of the individual pattern.

Such x-ray patterns also reveal information on the orientation and size distribution of crystallites. The average particle size D determined from the XRD pattern can be estimated from the Scherer's equation which is given by $D = k\lambda/\beta\cos\theta$, where k is a constant (shape factor, about 0.9), λ denotes the x-ray wavelength, β is the full width of half maximum(FWHM) of the diffraction line and θ is the diffraction angle.

X-ray techniques provide superior angular resolution and more accurate structural data than available from electron diffraction but over a large volume area of the sample. Figure 4.5 is showing the photograph of the x-ray diffractometer (model Bruker AXS D8 Advance) used during the preparation of this work.

The phase identification using x-ray diffraction depends on the positions of the peaks in the diffraction profile with relative to intensities at some extent. Another important aspect of the diffraction from the material is to consider how diffraction peaks change through the presence of various types of defects such as small number of dislocations in crystals with dimensions in millimeters.

The defects can be caused by the small grain size, which can change diffraction peak widths. The crystallite size is calculated as a function peak width (i.e. full-width at half maximum peak intensity, FWHM) peak position and wavelength.

4.2.3 Scanning Electron Microscopy

Scanning Electron Microscopy "SEM" is widely used to provide information on the elements which are present within the sample and is only one of the two techniques which provide elemental analysis. Taking into account the fact that SEM is suited for development of morphological imaging, it has been designed to detect signals which used to determine compositional information such as x-rays, back-scattered electrons, cuthodoluminesce, Auger electrons, and specimen current.

AFM and SEM are both commonly used for high resolution surface investigations. However, each of these tools resolves surface structure down to the nanometer scale. However, the image formation mechanisms are totally different, resulting in different types of information about surface structure.

The operation of the SEM consists of applying a voltage between a conductive sample and a filament, resulting in electron emission from the filament to the sample. The electrons interact within the sample few nanometers to several microns of the surface, depending on the beam parameters and sample type. Secondary electrons are the most frequently used signal for investigations of surface morphology. They are produced as a result of interactions between the beam electrons and weakly bound electrons in the conduction band of the sample.

The SEM image that is observed is basically the result of the intensity of the secondary electron emission from the sample at each x, y data point during the rastering of the electron beam across the surface. One of the key advantages of SEM with respect to the types of microscopy is its large depth of field. This allows it to image very rough surfaces wit millimeters of vertical information within a single image. The figure 4.6 shows the principle of SEM.

In light microscopy, a sample is viewed through a series of lenses that magnify the visible-light image. However, the scanning electron microscope (SEM) does not actually view a true image of the specimen, but rather produces an electronic map of the surface of the sample that is displayed on a cathode ray tube (CRT).

Electrons from a filament in an electron gun are beamed at the sample in a vacuum chamber. The beam forms a line that continuously sweeps across the sample at high speed. This beam irradiates the sample which in turn produces a signal in the form of either x-ray fluorescence, secondary or backscattered electrons. The Leo-StereoScan 440 Scanning Electron Microscope (SEM) unit used is shown in figure 4.6.

4.2.4 Atomic Force Microscopy

AFM provides a number of advantages over conventional microscopy techniques. AFMs probe the sample and make measurements in three dimensions, x, y, and z (normal to the sample surface), thus enabling the presentation of three-dimensional images of a sample surface. This provides a great advantage over any microscope available previously. With good samples (clean, with no excessively large surface features), resolution in the x-y plane ranges from 0.1 to 1.0 nm and in the z direction is 0.01 nm (atomic resolution).

AFMs require neither a vacuum environment nor any special sample preparation, and they can be used in either an ambient or liquid environment. With these advantages AFM has significantly impacted the fields of materials science, chemistry, biology, physics, and the specialized field of semiconductors.

AFM operate in three different modes: Contac mode; TappingMode and LiftMode. On Contact mode AFM is one of the more widely used scanning probe modes, and operates by rastering a sharp tip (made either of silicon or Si_3N_4 attached to a low

isolate mechanical and acoustical vibrations is also usually necessary to perform high resolution (atomic scale) work.

Recent advances in the development of AFM technology have led to a number of useful imaging modes including TappingMode and LiftMode AFM. Although operating in the contact mode has proven successful, it suffers from a number of drawbacks that limit its use on a number of sample types. First, the constant downward force on the tip often damages (and thus changes) many softer surfaces (polymers and biological samples) and even some hard surfaces such as silicon. Also, many samples, such as small particles or biological samples like DNA and cells must be placed on a substrate for imaging purposes.

In contact mode, the sample is often destroyed or even pushed out of the field of view by the rastering tip. These complications have been addressed through the development of TappingMode AFM.

In the TappingMode, the AFM tip–cantilever assembly oscillates at the sample surface while the tip is scanned; thus, the tip lightly taps the sample surface while rastering and only touches the sample at the bottom of each oscillation. This prevents damage to soft samples and avoids the "pushing" of samples around on the substrate. By using a constant oscillation amplitude, a constant tip–sample distance is maintained until the scan is complete. TappingMode AFM can be performed on both wet and dry sample surfaces.

LiftMode AFM provides the operator with a tool to record dual information about a sample surface at one location, such as topography and magnetic gradients (obtained in the magnetic force microscopy or MFM mode), thereby allowing the useful association of the two images.

The AFM images presented in this work are acquired by TappingMode by at the material research group of ithemba LABS.

LiftMode AFM operates by first scanning a line on the sample surface in TappingMode to obtain the topographical information. Then, the tip is lifted to a distance above the sample set by the operator and the same line retraced in a noncontact mode to obtain (for example) near surface magnetic field information. The process is repeated until the scan is complete and both images are saved. To perform MFM, a ferromagnetic tip and a ferromagnetic or paramagnetic sample are required. LiftMode AFM can also be used to record topography and electric fields or phase imaging data.

The continuing development of AFM technology provides scientists with a powerful tool to characterize a variety of sample surfaces. Minimal sample preparation, use in ambient conditions, and the ability to image nonconducting specimens at the atomic scale (in some cases) make AFM an extremely versatile and useful form of microscopy. Recent advances in AFM have allowed the successful imaging of soft polymeric and biological samples and the imaging of magnetic microstructures.

4.2.5 Electrical Characterization: Four-Point Collinear Probe   Method for Resistivity

The most common way of measuring the resistivity of a material is by using a four-point collinear probe. This technique involves bringing four equally spaced probes in contact with a material of unknown resistance. The probe array is placed in the center of the material, as shown in Figure 4.8. The two outer probes are used for sourcing current and the two inner probes are used for measuring the resulting voltage drop across the surface of the sample.

thereby raised the vibrational state of the molecule or created a phonon) is denoted as the Stokes shifted light. Light which has gained energy (and lowered the vibrational state of the molecule or annihilated a phonon) is the Anti-Stokes shifted light.

Because it is applicable to materials in solid, liquid, and vapor phases, the applications of Raman spectroscopy span several fields. The most obvious is the non-intrusive identification of organic and inorganic species for which the unique, vibrational 'fingerprint' of the molecule is known. Because the Raman scattering intensity is proportional to the number of molecules in the sampling area relative concentrations of solutes can be learned. If special care is taken and the Raman scattering cross sections are known then absolute concentrations and densities are derivable [3].

The inverse application in structural chemistry is of course also possible; Raman spectra and polarization analysis (or orientation dependence of scattering intensities in crystalline structures) can be used to deduce the symmetry and structure of a sample.

Information on the effects of temperature, pressure, stress, and environment on a molecule or solid is gained by measuring the changes in shape, energy, and intensity of Raman bands [4].

Special Raman techniques continue to develop which are tailored to the particular applications. Many of these new techniques are possible due to the continuing improvement of laser sources, focusing and collection optics, high resolution wavelength dispersers, and sensitive detectors.
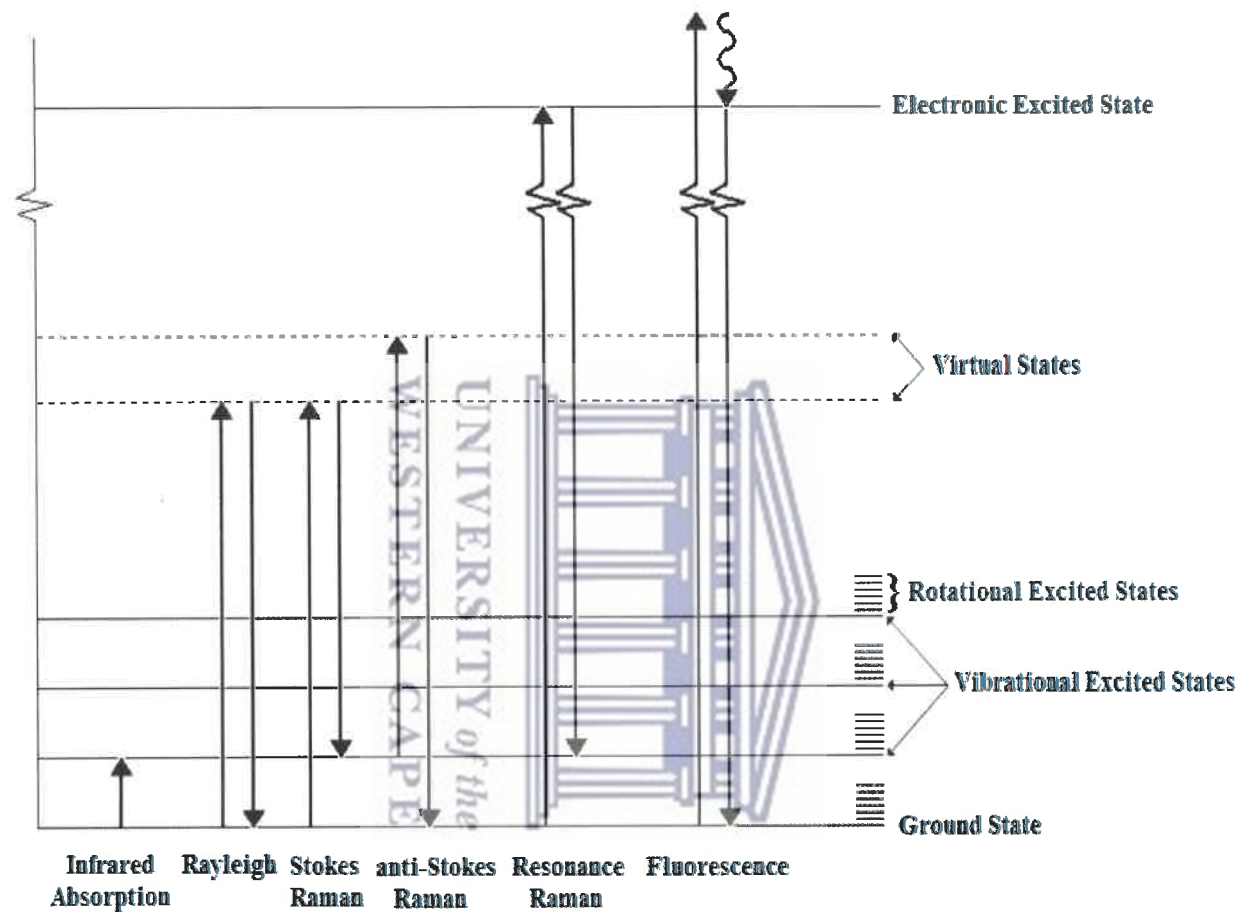
Figure 4.9

Schematic of the quantized vibrational, rotational, and electronic energy levels of a molecule.

103

interesting effects occurring at various times of the expansion and at different pressure levels.
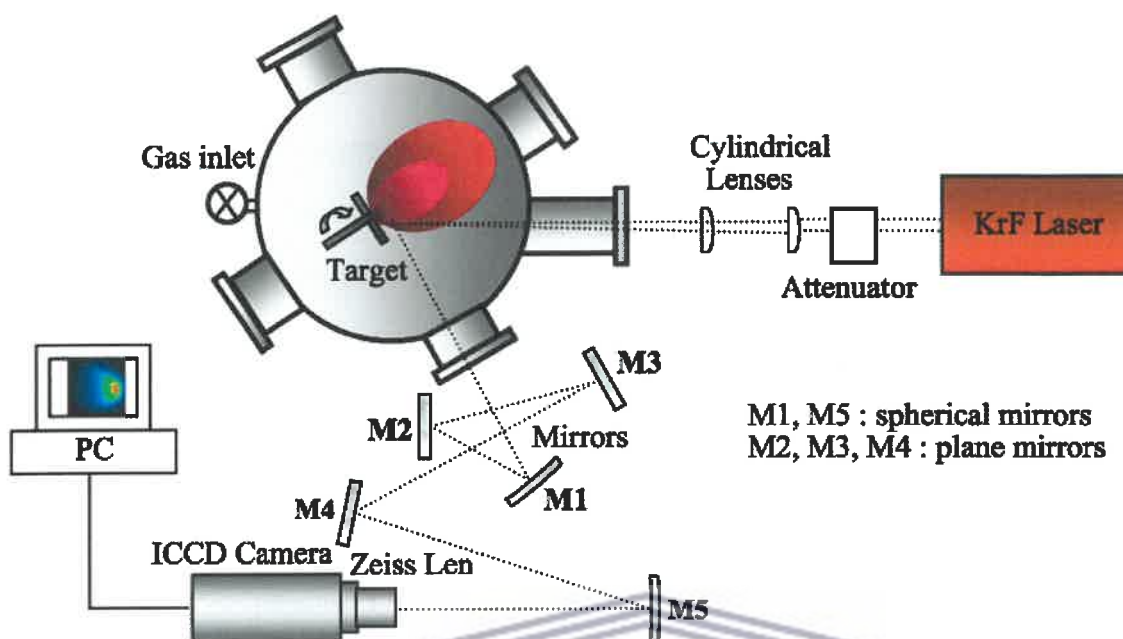
Fig. 4.10

Schematic of the experimental set-up of the ICCD–based Fast photography of the plume expansion

4.3 CONCLUSION

A summary of the description of all the used technique have been done. Thus we are going to examinate the effect the different parameters on the properties of the $Sm_{0.55}Nd_{0.45}NiO_3$ nanostructures thin film which will be the focus of the next chapter.

4.4 Bibliography

[1]   A. Smekal, Naturwissenschaften, 11, 873 (1923).

[2]   C. V. Raman and K. S. Krishanan, Nature, 121, 501, (1928).

[3]   H. W. Schrotter and H. W. Klockner, in Raman Spectroscopy of Gases and Liquids, edited by A. Weber (Springer –Verlag, Berlin, 1979) p.123.

[4]   D.A. Long, Raman Spectroscopy (McGraw-Hill Inc., London, 1977).

doped and undoped silicon "Si", Aluminium lanthanate "LaAlO$_3$", strontium titanate "SrTiO$_3$" and NdGaO$_3$ (NGO) substrates using a pulsed excimer laser sources.

The deposition parameters of Sm$_{0.55}$Nd$_{0.45}$NiO$_3$ nano-structures by PLD described in this work are summarized in Table 5.1a. The deposition condition was optimized to ensure that we meet the best conditions that stabilizes the Sm$_{1-x}$Nd$_x$NiO$_3$ at x= 0.45 solid solution, whereas some of the parameters were changed for comparison purpose.

In this work we present both published and new experimental data about the stabilization of Sm$_{1-x}$Nd$_x$NiO$_3$ at x= 0.45 solid solution. The results are reported and discussed in the framework of a specific aspect focusing at the best conditions that subject to optimize the synthesis of Sm$_{1-x}$Nd$_x$NiO$_3$ at x= 0.45 solid solution .

In particular we report on some structural, microstructural and fast photography imaging studies of the plasma generated by the KrF excimer laser ablation of Sm$_{1-x}$Nd$_x$NiO$_3$ at x= 0.45 in the presence of oxygen background gases at different pressures. The experimentally determined behaviours are compared with the predictions of an analytical model which gives a complete description of the expansion of the plume and with some recent results reported in the literature. Evidences of the strong influence of the expansion plasma regime were found which showed that it is not simply related to the overall reactive gas content.

5.1 Effect of the Substrate

The pure $Sm_{0.55}Nd_{0.45}NiO_3$ nanostructured thin films were deposited onto Corning glass, doped and undoped silicon "Si" substrates using pulsed excimer laser sources. The deposition conditions are summarized in the Table 5.1b. In this section we report on the effect of the substrate nature on $Sm_{0.55}Nd_{0.45}NiO_3$ films on its composition, crystallography, surface morphology and electrical properties grown by PLD technique.

5.1.1 Thickness and composition determination

In this experiment a target with the composition of $Sm_{0.55}Nd_{0.45}NiO_3$ was used to grow different films of the same concentration on different substrate. Figure 5.1 shows a typical RBS spectrum of $Sm_{0.55}Nd_{0.45}NiO_3$ on Corning 1737F glass substrate sample. For ease of reference, the nickelate will henceforth be referred to as $Sm_{0.55}Nd_{0.45}NiO_3$ and corning 1737F glass substrate will be referred to simply as glass substrate. The solid line through winkled data set is the simulation of the spectrum using RUMP and Genplot software.

From the simulation of the films grown on different substrate, one can determine the thickness and the composition. The thickness of $Sm_{0.55}Nd_{0.45}NiO_3$ layer shown in table 5.2 was estimated to be 711.8 nm, 698.0 nm, 852.6 nm, and 851.9 nm for the film grown on corning glass, and Si(100) oxidized p-doped, Si(100) p-doped, Si(111) native SiO_2 and Si(111) HF etched leading to growth rate of 11.86, 11.63, 14.21 and 14.19 nm/min respectively. With an inaccuracy of 2-5% [1] in RBS and taking an inaccuracy of 5% all the samples were found to exhibit the same elemental concentrations irrespective of the substrate nature; oxygen (55.1±2.8) at %, Ni (21.8±1.1) at %, Nd (10.1±0.5) at % and Sm (13.0±0.6) at %.
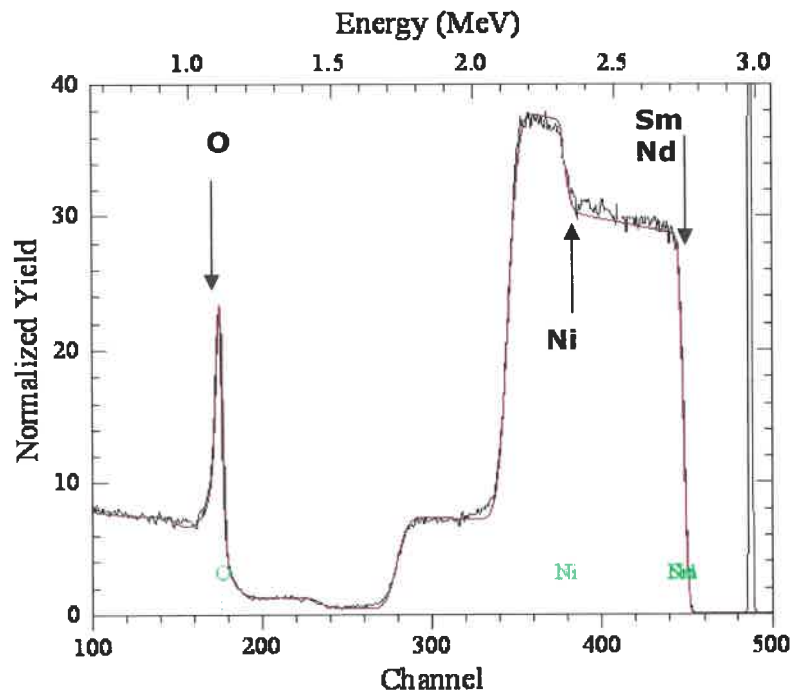
Figure 5.1

Rutherford Backscattering spectra for 3.05 Mev He$^+$ ions incident on the $Sm_{0.35}Nd_{0.65}NiO_3$ films grown on corning glass

Sample	Thickness (A)	Comp: Sm%	Comp: Nd%	Comp: Ni%	Comp: O%
on Corning glass	7118	13.0	10.1	21.8	55.1
On Si(100) oxid P doped	7118	13.0	10.1	21.8	55.1
On Si(100) P doped	6980	13.0	10.1	21.8	55.1
On Si(111) native SiO2	8526	13.0	10.1	21.8	55.1
On Si(111) HF Etched	8519	13.0	10.1	21.8	55.1

Table 5.2

Films thickness and composition dependence on the nature of the substrate.

111

(100). This suggests that the Bragg's reflections are broadened because of the presence of a large distribution of the lattice parameters in the films, or more appropriately, to the small differences in stoichiometry across the samples due to lack of oxygen.

These results also reveal a clear displacement of the reflection (111) to higher 2θ values for the sample deposited in glass substrate. Such a displacement indicates that change in substrate results in a shrinkage of the unit cell volume. This expected behaviour is due to the significant lattice mismatch between the film and Si and Glass substrates.

This behaviour also can result in the luck of oxygen as demonstrated by RBS analysis; in fact the presence of an unstable Ni^{3+} oxidation state implies the possibility of large oxygen nonstoichiometry for $ReNiO_3$. The boundary of the oxygen nonstoichiometry range and structural changes, caused by an oxygen deficiency, were reliably determined for $NdNiO_{3-\delta}$ and $SmNiO_{3-\delta}$ [2].

The oxygen nonstoichiometry can greatly affect the structural, magnetic and transport properties of the nickelates. An increase of oxygen deficiency in $LaNiO_{3-\delta}$ causes changes in resistance, magnetoresistance, magnetic susceptibility, Hall and Seebeck coefficients [3, 4]. Moreover, an oxygen nonstoichiometry can be of considerable importance for $ReNiO_3$ thin films, which are perspective materials for various electronic applications [5]. Along with oxygen deficiency, cation nonstoichiometry is possible for these compounds because the lack of rare-earth cation can be compensated either by the formation of oxygen vacancies or by equivalent rise of Ni^{3+} content.

113

I.V. Nikulin et al [2] study the dependence of the lattice constants and unit-cell volume versus the oxygen content for $NdNiO_{3-\delta}$ and $SmNiO_{3-\delta}$. They suggest that the high uncertainties in lattice-constant values for the $NdNiO_{2.80}$ and $NdNiO_{2.71}$ compositions are due to the relatively low synthesis temperature (700 and 800 °C, respectively), which results in a small crystallite size and, therefore, in a broadening of the diffraction peaks.

Nevertheless one could expect an increase of the lattice-constant values with decreasing oxygen index due to the reduction of a certain portion of Ni^{3+} to Ni^{2+}, which has a bigger ionic radius, giving rise to the formation of the others phase formed in the samples.

5.1.3 Morphological properties: SEM and AFM analysis

Film morphology describes atoms arrangement in a material. The Scanning Electron Microscope and Atomic Force Microscope are known to be suited for providing information about the morphology of the film. The surface morphology of the different samples deposited on different substrate investigated by mean of SEM and AFM, shows a net dense film structure with several droplets population [Figure 5.3, Fig 5.4]. The nano-scaled droplets are in general spherical in shape.

The formation of these droplets is very difficult to avoid in Laser ablation, hhowever the comprehension of cluster formation and deposition and of the first stages of film formation (as a function of cluster size and energy) plays a fundamental role for the control of the film and surface properties.

A variety of cluster deposition regimes have been extensively studied by means of theoretical models and experiments, mainly investigating the role of cluster deposition kinetic energy and, to some extent, of cluster size distribution [6, 7, 8-21]. It has been demonstrated that high energy deposition (i.e. several eV/atom

onto the surface, if not able to properly transfer their energy to the substrate, can even melt [7] and, after diffusion, coalesce. In fact molecular dynamics simulations [7, 8, 9, 12] show that highly energetic cluster impacts generate a pressure shock wave and a transfer of the cluster kinetic energy to the substrate, followed by a very high local temperature increase.

The coalescence between 'liquid' clusters is a process requiring energy, since it involves dislocation phenomena, elastic stress and formation of new chemical bonds as shown by Zhu and Averback for Cu clusters [31]. The resulting larger clusters then cool and become 'solid' in the most energetically favorable configuration, i.e. spherical. Ablation and deposition of species with a high kinetic energy lead to penetration in the surface, and to diffusion/coalescence.

It is likely that the mobility of $Sm_{0.55}Nd_{0.45}NiO_3$ species on glass is a little bit smaller than on Si, and that most of the aggregates observed on the glass surface are formed in the plume before impact on the substrate, not being (at least most of them) the result of a post-deposition surface aggregation.

This is evidenced by deposition on Si substrate, where irregular, ramified aggregates are observed, composed by juxtaposed substructures having nearly the same size as clusters observed on glass substrates, as confirmed by a statistical analysis of their size distribution.

The SEM images in fig.5.3 reveal that the small clusters arriving at the glass and Si substrates surfaces (and formed in the ablation plume in the same conditions) have the same size, corresponding to clusters composed by a few hundred atoms.

117

During the deposition the clusters only stick to other clusters probably because they overcome a critical size above which coalescence is no longer favored and/or they do not possess enough energy to remain in the liquid phase [7]; probably both a smaller kinetic energy and a larger average cluster size lead to the described process. This kind of growth has been largely studied in the literature both experimentally and with theoretical models (DDA, Deposition- Diffusion-Aggregation [6, 14, 15]).

Therefore, differences between structures observed on Si and glass in the same deposition are a consequence of the different mobility of the species on these substrates. The small clusters particles observed on Si and glass substrates are clusters formed in the ablation plume which impinge onto the substrates surfaces and experience a negligible diffusion, maybe also because some of them may be partially implanted. In fact, the cluster aspect ratio (between diameter and height) is about 2, i.e. clusters are flattened, suggesting not negligible impact energy, or at least a complex cluster-substrate interaction.

This observation opens the way to the study of the size distribution of clusters resulting from ablation in different conditions (e.g. different gas pressure) by observation of deposits on a flat substrate where the mobility is strongly reduced. The reported behavior shows the fundamental role of the substrate when investigating species formed in the ablation plume, i.e. observed isolated structures on surfaces are deeply influenced by interaction with the substrate itself.

Anyway, this effect should also vanish in film growth with increasing deposited material and above a certain film thickness.

5.1.4 Electrical properties

Since the discovery of the first-order metal-insulator transition in orthorhombically distorted perovskite oxides of the general formula $ReNiO_3$ (Re=rare earth), a great number of studies have been performed in order to better understand their general physical properties [32, 33]. Measurements of electrical resistance versus temperature on these compounds reveal the occurrence of a MI transition in a rather large range of temperature. In fact, the metal-insulator transition temperature (T_{MIT}) associated with such a transition was found to rise systematically as the size of the rare-earth ion decreases, being 135, 200, 400, & 560 K for pure Re= Pr, Nd, Sm & Gd respectively [34]. These results also suggested that the MI transition is microscopically related with the degree of distortion of the ideal perovskite structure.

The superior advantage of this nickelate materials family relatively to the standard MIT Mott type oxides such as vanadium oxides is the controllability of their T_{MIT}. The shift of their T_{MIT} can de precisely regulated by the choice of the lanthanide cation; a smaller cation induces a distortion of the Ni-O-Ni angle from 180°, and therefore the metal-insulator occurs at higher temperature. This remarkable property of these high temperature stable perovskites in the ability to tune the T_{MIT} is achieved by forming a solid solution $Re_{1-x} Re'_x NiO_3$ and adjusting the relative ratio of the cations constituting the solid solution.

To perceive directly the targeted T_{MIT} phenomenon at around 37°C, 4 and 2 points probe resistance investigations were carried on all the $Sm_{0.55}Nd_{0.45}NiO_3$ deposited films in the range of 25-100°C because of lack of low temperature measurements equipments.
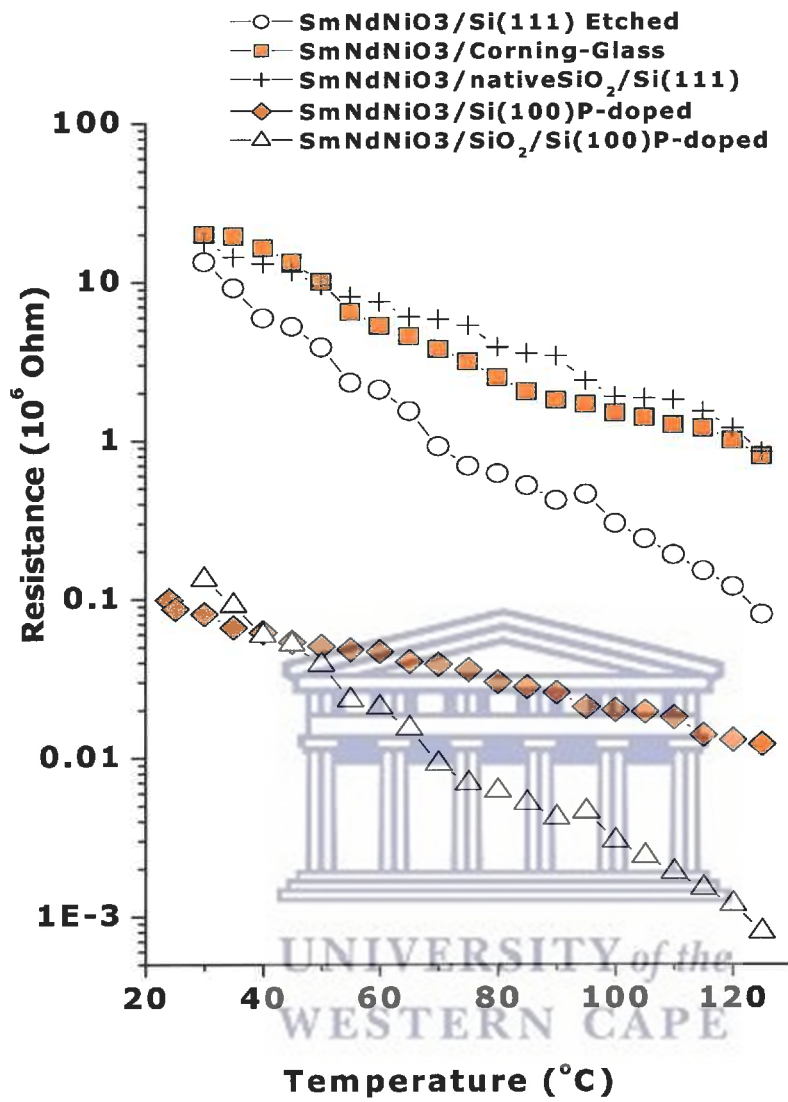
Figure 5.5

Evolution of the Resistivity of the sample grown on different substrate

undoped Si (100) by varying the background oxygen pressure and keeping the substrate target distance constant at 3.0 cm.

5.2 Effect of the Oxygen pressure

In this section we report on the effect of oxygen pressure on $Sm_{0.55}Nd_{0.45}NiO_3$ films on its crystallography and surface morphology grown by PLD technique on Si (100) substrate. The dependence of structural and morphological of the grown films on the oxygen deposition pressure was investigated. The structures of the films were studied using X-ray diffraction analysis (XRD), Raman spectroscopy and the surface morphology using scanning electron microscope (SEM) and atomic force microscopy (AFM).

5.2.1 Structure and morphology

Film morphology describes atoms arrangement in a material. Crystallinity on the other hand is an ordered arrangement of atoms. An amorphous material does not exhibit crystallinity whereas polycrystalline materials posses short range of crystallinity. Polycrystalline areas are known as grains and very small in size depending on processing parameters.

Grain size is known to be a very important feature that can significantly influence the mechanical, physical properties of the material.

The Scanning Electron Microscope and Atomic Force Microscope are suited for providing information about the morphology of the film. It is well known that the intrinsic properties of $Sm_{0.55}Nd_{0.45}NiO_3$ strongly depend on the morphology, and size of its crystallites, that is why the properties of high surface area $Sm_{0.55}Nd_{0.45}NiO_3$ have attracted most scientific attention.

125

group symmetry. The results reveals a strong orientation along the (120) reflections of the perovskite subcell as illustrated in fig.5.6c. The figure 5.6c displays all the reflections belonging to the solid solution $Sm_{0.55}Nd_{0.45}NiO_3$ phase except the one corresponding to (110), (113) and (040) which appears only in fig 5.6a and 5.6b. These peaks are much sharper and stronger than the same ones displayed in Figs. 5.6a and 5.6b as illustrated in fig 5.7a.

X-Ray Diffraction is used to determine the type of crystallinity in the $Sm_{0.55}Nd_{0.45}NiO_3$ films. X-Ray diffraction may show these films are polycrystalline. However in general terms, the crystal plane with the highest atomic density exhibits the lowest surface free energy. This is due to the fact that this crystal plane somehow favours a subsequent preferential growth. Preferential crystal growth is also strongly affected by the synthesis parameters or lattice mismatch between the film and substrate. It is well known that the film has the tendency to grow by reducing the overall film energy.
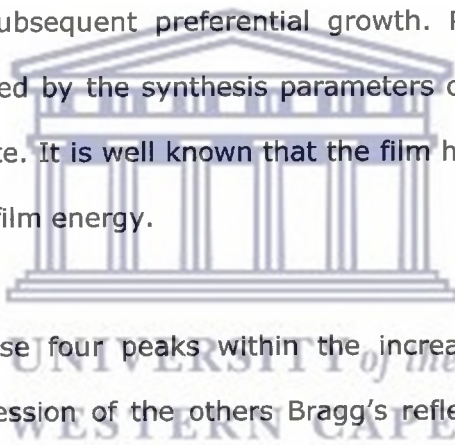
The only observation of these four peaks within the increase of the oxygen pressure indicates the suppression of the others Bragg's reflections of the film, showing the preferential growth along these planes as illustrated in Fig 5.7a. The observed (120) peak intensity which is corresponding to the d_{hkl} value of about 2.358 Å, increases and its position shifts to the right for the film grown under 0.2 mbar oxygen pressure and then slightly to the left for the film grown under 0.4 mbar oxygen pressure [table 5.3]. Fig. 5.7b shows clearly these oxygen pressure dependence features for (120) crystal plane growth. The intensity of (120) peaks is much stronger for the sample grown under 0.4 oxygen pressure and gets suppressed by decreasing oxygen pressure.

The $d_{(120)}$ as well as the crystalline size (D_{120}) along the (120) plane growth of the samples which was determined from the positions and full width at half
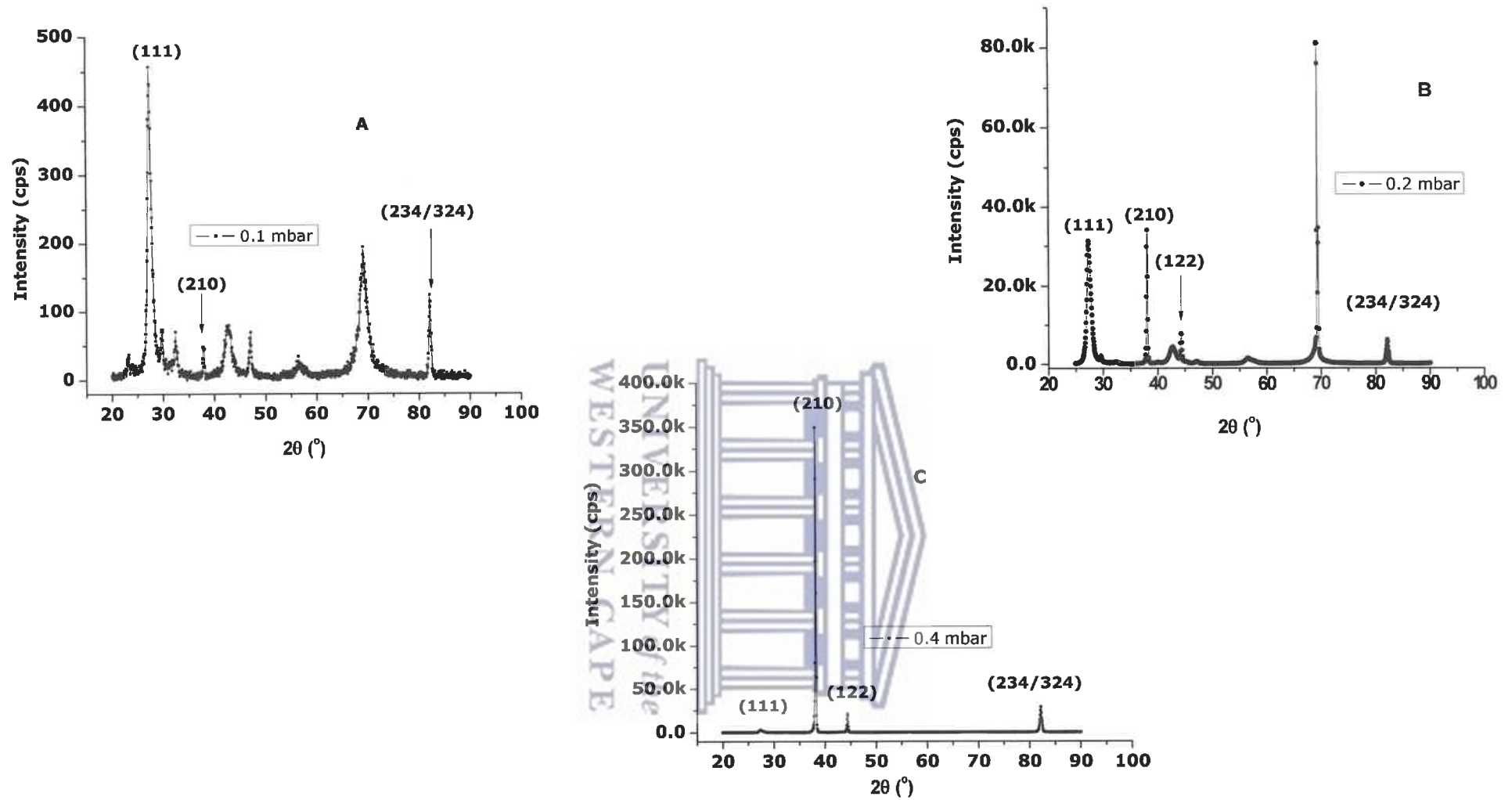
Figure 5.6

XRD diffactogram of $Sm_{0.55}Nd_{0.45}NiO_3$ thin films deposited on pure Si (100) substrate with different O_2 pressure.

Figure 5.8 shows the SEM images of the $Sm_{0.55}Nd_{0.45}NiO_3$ films deposited on pure Si (100) with different oxygen pressure. The $Sm_{0.55}Nd_{0.45}NiO_3$ films with high O_2 pressure behave differently from those with lower oxygen pressure. For instance, a film with lower oxygen pressure leads to regular small grains which are uniformly dispersed on the surface. On the other hand, film with high O_2 pressure the grains size still uniform but tend to be bigger in size as demonstrated from the XRD results. The formation of spherical nano-clusters is also observed in the SEM images where their sizes seem to be independent of the oxygen pressure.

Surface morphology and roughness were evaluated using an Atomic Force Microscope "AFM" as shown in Figure 5.9 an analysis of these data permitted us to agree with the results obtained from SEM. The low roughness values also confirm the good homogeneity of these films. There is no clear cut correlation between the roughness values obtained and the oxygen pressure as shown in Table 5.3, but what is obvious is the fact that films deposited with 0.2 mbar of O_2 have the lowest roughness value.

The formation of nanoclusters observed in both SEM and AFM images where their sizes seem to be independent within the increase of the oxygen pressure reveal an important characteristic of the interaction of these nickelates compounds with laser beam.

The geometrical structure of the nanoclusters self-assembled on the substrate surfaces under pulsed laser deposition (PLD) has been experimentally investigated [38]. The PLD technique is characterized by an extremely high instantaneous deposition rate. Unlike for the thermal evaporation (TE) process, formation of fractal nanoclusters under PLD conditions has been observed with scanning tunneling microscopy (STM) [38].
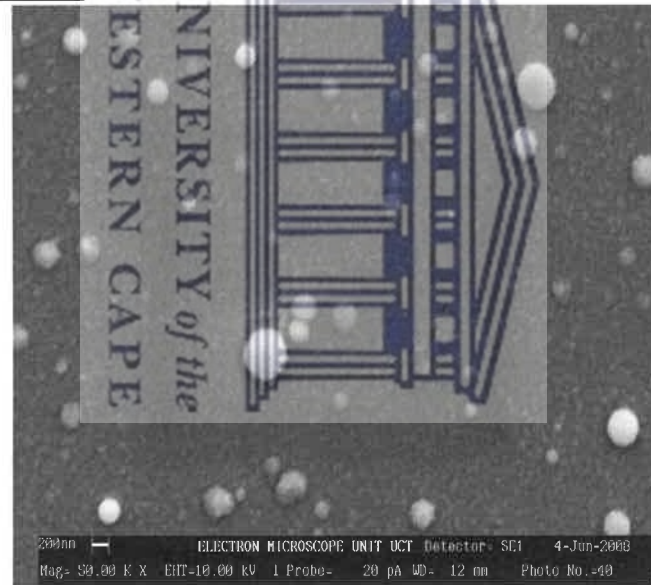
0.1 mbar
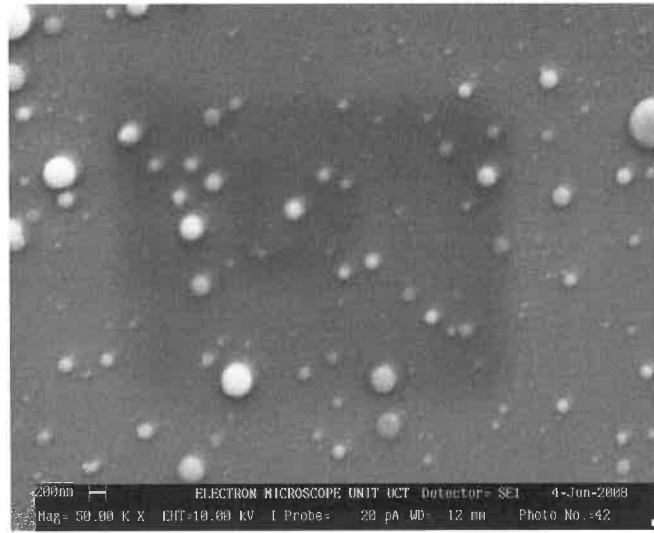
0.2 mbar
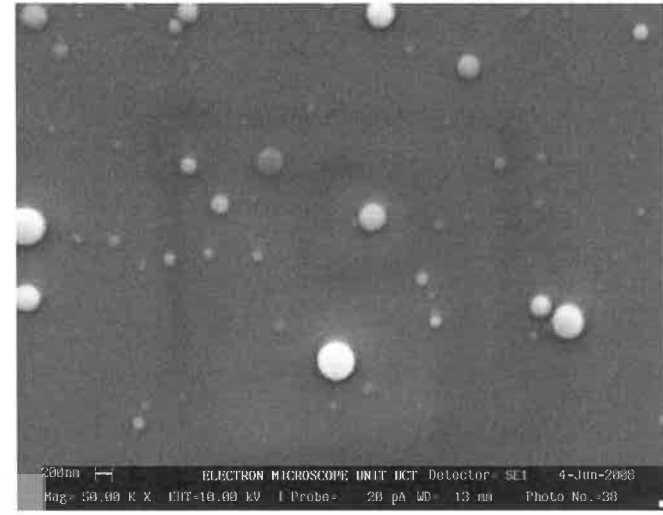
0.4 mbar

Figure 5.8

Evolution of the SEM images with the O_2 pressure of the film growth on Si (100)

133

Oxygen Pressure (mbar)	D_{111}(Å)	d_{120}(Å)	d_{122}(Å)	$d_{234/324}$(Å)	$FWHM_{120}$(°)	D_{120}(Å)	Roughness (nm)
0.1	3.255	2.377	not detected	1.173	0.4	209	4.96
0.2	3.252	2.358	2.042	1.172	0.24	350	2.62
0.4	3.148	2.359	2.040	1.172	0.18	466	6.38

Table 5.3

Structural parameters and grains size of the sample grown on Si (100)
with different O_2 pressure

Moreover the kinetic energies of the plume species (atoms, clusters, etc.) and are only representative of the cluster deposition kinetic energies. In any case this energy is indeed compatible with the observed different cluster behavior on surfaces ranging from implantation to mobility and aggregation, also depending on the substrate surface properties; it will be very interesting in investigating the clusters coalescence and aggregations by depositing for a long time and also to better probe the crystallinity of the films and to reduce the broadening of the xrd peaks, it would be very interesting in depositing in a perovskite substrate to minimize the substrate films lattice mismatch.

Thus the following section deal with the effect of deposition time on structural and morphological properties of $Sm_{0.55}Nd_{0.45}NiO_3$ films deposited on $NdGaO_3$ (110) single crystal perovskite substrate.

5.3 Effect of the deposition time

In this section we report on the effect of deposition time on $Sm_{0.55}Nd_{0.45}NiO_3$ films on its crystallography, surface morphology and Raman properties grown by PLD technique on $NdGaO_3$ substrate. The dependence of structural, morphological and Raman of the grown films on the deposition time was investigated. The structures of the films were studied using X-ray diffraction analysis (XRD), Raman spectroscopy and the surface morphology using scanning electron microscope (SEM) and atomic force microscopy (AFM).

5.3.1   Structural properties
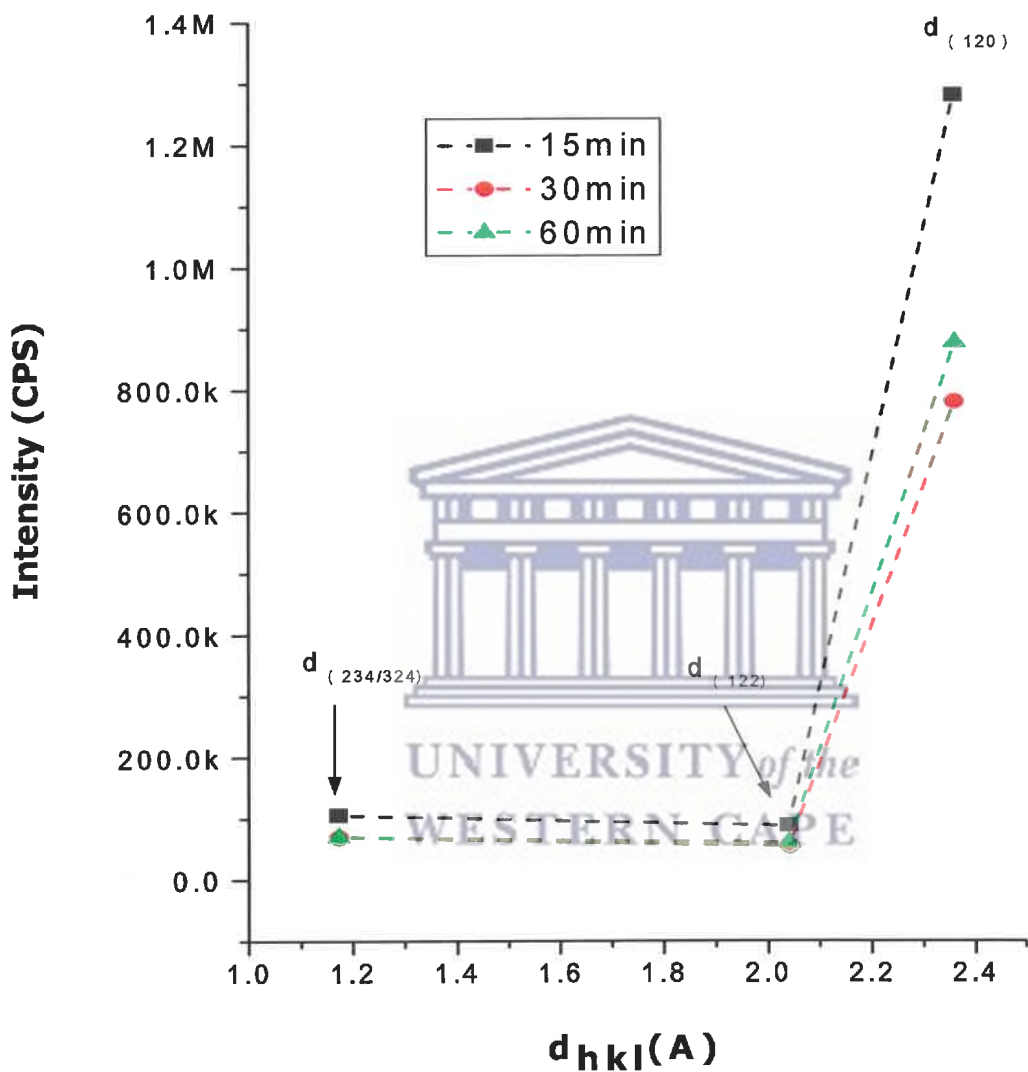
Figure 5.11 shows the typical X-ray diffraction patterns for $Sm_{0.55}Nd_{0.45}NiO_3$ nanostructured thin film grown on $NdGaO_3$ substrate (its diffraction patterns is presented in figure 5.10) with different deposition time under an O_2 pressure of 0.2 mbar.
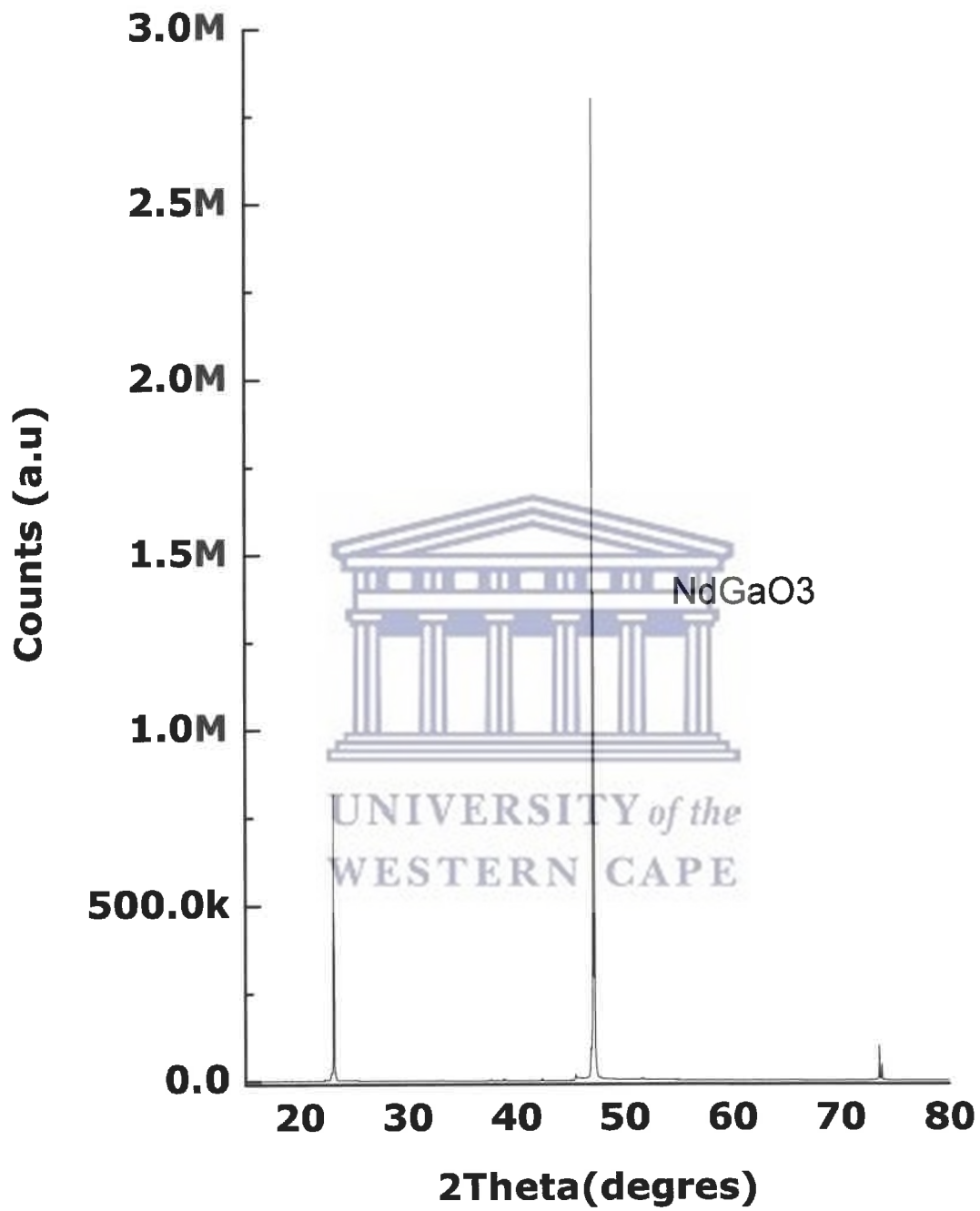
Figure 5.10

XRD diffactogram of NdGaO$_3$ (110) bulk single crystal substrate

139

Figure 5.12

Evolution the intensity of the Bragg's Reflections of $Sm_{0.55}Nd_{0.45}NiO_3$ thin films deposited on pure $NdGaO_3$ substrate with different deposition time.

141

5.3.2   Morphological properties

5.3.2.1   SEM analysis

Scanning Electron Microscopy is used at room temperature to study the surface topology, and provides information on $Sm_{0.55}Nd_{0.45}NiO_3$ films growth. Usual films produced by PLD method at low or very high temperature contains some macroscopic particulates hence the results indicates that the surface of the films is rough except for the films deposited for 15 min, this is also approved by the surface roughness average $R_a > 30$ nm.

The typical SEM images of the grown $Sm_{0.55}Nd_{0.45}NiO_3$ films are shown in figure 5.14 the films show remarkably different morphologies for different deposition time. As a comparison, Fig. 4.14 shows the morphology of $Sm_{0.55}Nd_{0.45}NiO_3$ grown on $NdGaO_3$ with different deposition time.

The view reveals that they are composed of numerous nanocrystals highly packed on the substrate for the samples grown with a deposition time of 60 min. The samples have a granular morphology and the grains become more uniform, bigger in size as the deposition time increase from 15 min to 60 min. Considerable nano-scaled droplets in general spherical in shape related to the laser ablation are observed on all the samples.

5.3.2.2 AFM analysis

The result on the study of the surface morphology as function of the deposition of the $Sm_{0.55}Nd_{0.45}NiO_3$ films depicted in figure 5.15 shows the 2D AFM images, and may be correlated to the previously studied SEM images. At high deposition time, the AFM images show a high grain density. Grains are tightly packed, and the size of irregular grains for the films grown during 60 min.
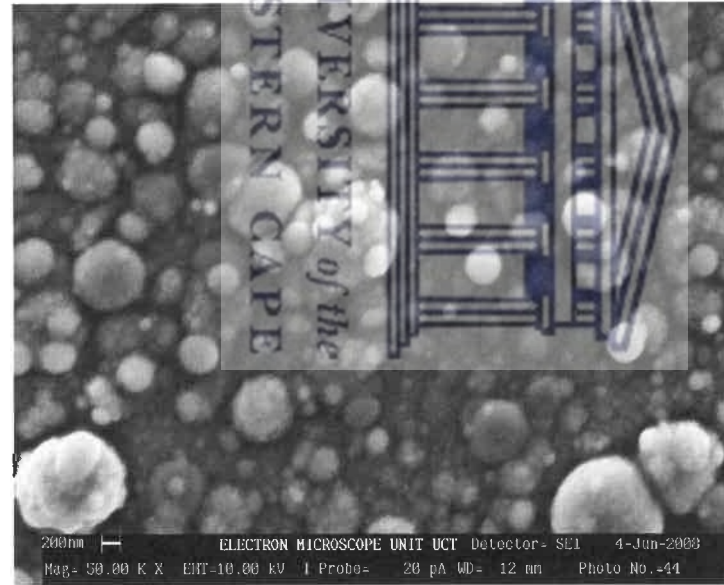
143

15 min
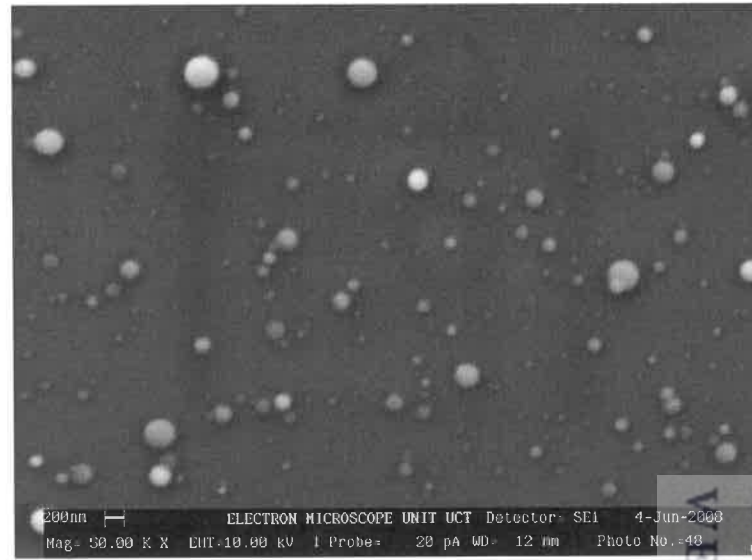
30 min
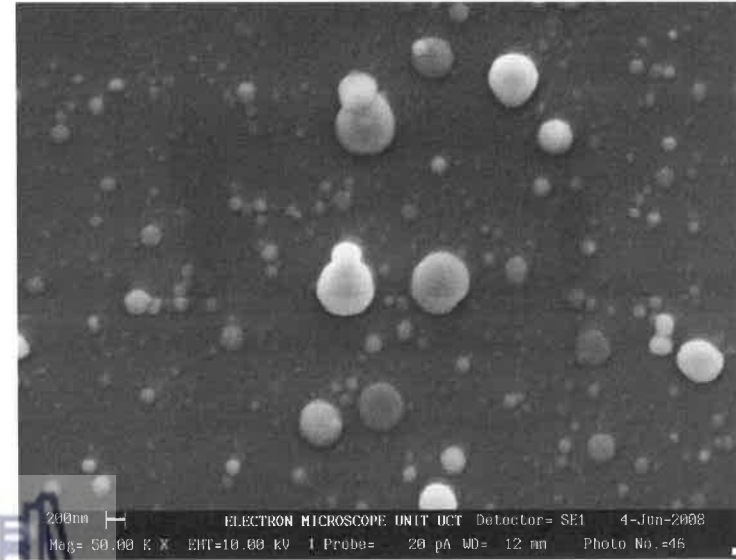
60 min

Figure 5.14

Evolution of the SEM images with the deposition on the film growth on NdGaO$_3$

145

In this work has been noticed that the surface roughness of the $Sm_{0.55}Nd_{0.45}NiO_3$ films depend on the deposition conditions, at low deposition time the surface roughness is low and show that the films are highly crystalline. As the deposition time increases the surface roughness is increasing and the films become less crystalline, the surface roughness is very high compared with sample deposited for 15 min, this might caused by the long re-exposure of the $Sm_{0.55}Nd_{0.45}NiO_3$ films to the plasma. It is also assumed that the high surface roughness R_a might cause by high concentration of clusters in the sample, which is induced by the coalescence of the nanodroplets.

5.3.3 Raman spectroscopy

The measurements by Raman spectroscopy were conducted at room temperature using Ar laser of the excitation wavelength 514.5 nm, whereby the detector uses liquid nitrogen to cool Ge diode detector at the resolution 4 cm^{-1} , with zero filling factor.

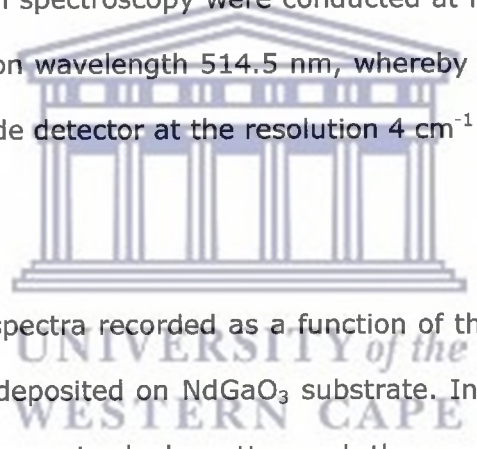Fig. 5.18 shows the Raman spectra recorded as a function of the deposition time of $Sm_{0.55}Nd_{0.45}NiO_3$ samples deposited on $NdGaO_3$ substrate. In spite of different conditions of preparation, the spectra look pretty much the same for the samples deposited during 15 and 30 min. They contain the same lines all probably coming from the substrate, the most significant difference concerns the sample deposited during 60 min where a broad line in the vicinity of 496 cm^{-1} was only observed and this line is attributed to the film.

The observed difference is attributed to the fact that the latter is thicker than the formers and that the vibration of the substrate is very sensitive as it a single crystal.

Figure 5.16

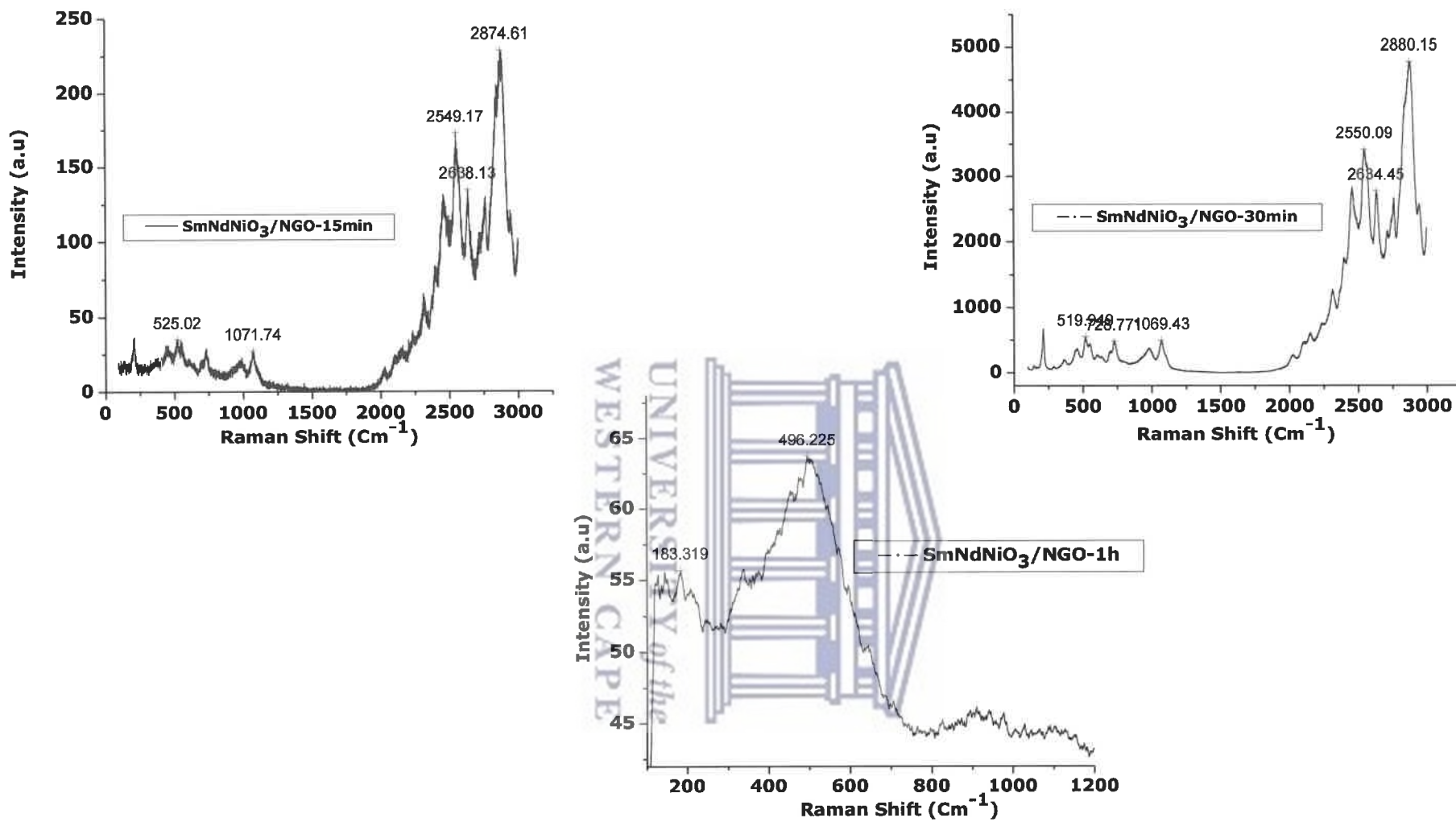Raman shifts of $Sm_{0.55}Nd_{0.45}NiO_3$ thin films nanostructured deposited on $NdGaO_3$ substrates with different deposition time

5.3.5 Conclusion

We presented in this section a complete study of the evolution of the crystalline state, surface morphology and the thermal evolution of the resistivity of PLD grown $Sm_{0.55}Nd_{0.45}NiO_3$ films on $NdGaO_3$ substrate as a function of the deposition time. The direct dependence of deposition time of the evolution of the structural and morphological properties of the PLD grown $Sm_{0.55}Nd_{0.45}NiO_3$ films on $NdGaO_3$ were demonstrated, and confirm the results obtained on Si and glass substrates.

The $Sm_{0.55}Nd_{0.45}NiO_3$ is directly obtained as single phase; films systematically present only one phase corresponding to the stabilisation of the $Sm_{0.55}Nd_{0.45}NiO_3$ solid solution and the corresponding surface presents a roughness which is increasing with the deposition time. The direct stabilisation of the $Sm_{0.55}Nd_{0.45}NiO_3$ phase without any additional may be due to the epitaxial growth of the film on $NdGaO_3$ substrate.

However, the influence of the deposition time on the MI transition does not appear to be straightforward because of lack of experimental details. The thermal evolution of the resistivity of the films under different conditions is thought to be highly related to their thermal history in the PLD process which always reveals the presence of nano-scaled droplets. These late droplet affect the microstructure of the films and therefore destroy their physical properties. However no clear relationship between these parameters has been found yet and further work is needed in order to elucidate it.

The nano-scaled droplets are in general spherical in shape which indicates that the laser ablation of this nickelate family is governed at a certain extent by a heat transfer phenomenon. For an accurate description of the ablation process, a comprehensive study of the plume dynamic is there required.

151
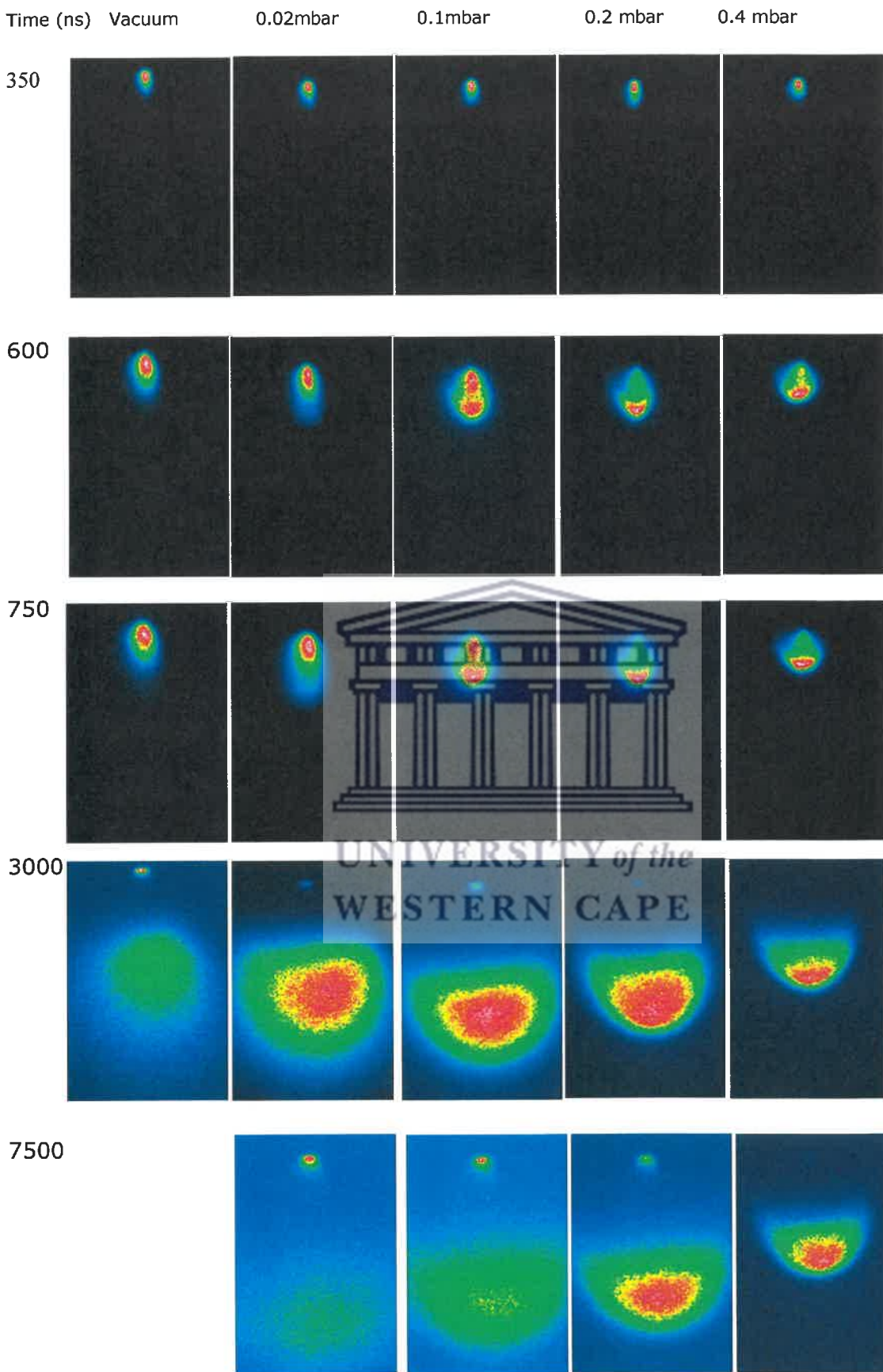
Figure 5.18

The temporal evolution of the visible plume. The position of the ablating surface is at the limit of the top side of the images

153

In order to study the plasma plume expansion dynamics, we have plotted the plume luminous front position versus time delay at different pressures (see Fig. 5.19). By increasing the oxygen pressure, the expansion remains linear in the early time. From vacuum to 0.2 mbar no significant change in the initial velocity was observed. We estimated this velocity to be around 1.79×10^6 cm/s. From 0.3 to 0.8 mbar the initial velocity decreases from 1.65×10^6 to 1.39×10^6 cm/s.

As the time evolves a deviation from free-plume expansion occurs and the plume slows down. In this regime of propagation, the ejected species collide with gas molecules and loss their kinetic energy. Later, the plume front stops completely (Fig. 5.19). At this stage, the ejected species diffuse into the ambient gas until they reach a distance where they loss completely their kinetic energy. The transition from one expansion regime to the following occurs at different time delays and distances depending on the gas pressure.

Several models have been proposed to describe the ablation plume expansion in a background gas. The deviation from the free-plume expansion and the appearance of luminous layer in the plasma-gas interface marks the presence of a shock wave front. We used different model (as described in Chapter III section 3.4) to fit our experimental data in order to verify their validity. The results are shown in Figure 5.20 and the fitting parameters are reported in Table 5.4.

It was found that for all used pressures the shock wave model fit agree well only with some of our experimental data and in a range of pressures. At 0.2, 0.3, 0.4 and 0.8 mbar the lower limit of the deviation from the free-plume expansion to the shock-wave-like expansion, is 09, 8.15, 8.06 and 9.5 mm, respectively. At lower pressures, the shock wave model does not fit well with our experimental data but the drag model agreed well from the deviation of a free-plume expansion.

155
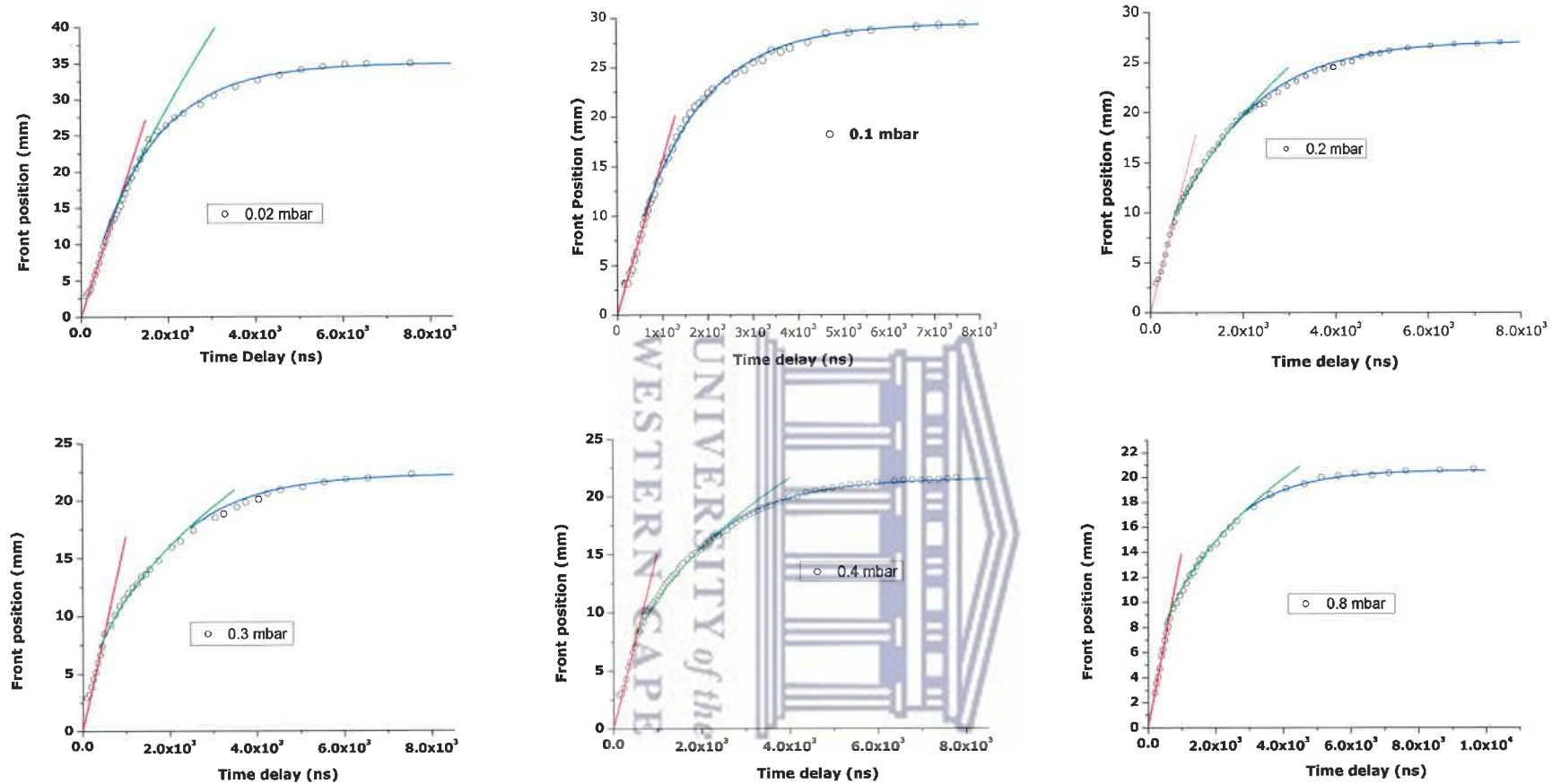
Fig. 5.20

Fits of the different models used to describe the plume expansion for different pressures. The *red line* represents the free expansion. The *green line* shows the shock-wave model fit. The *blue line* shows the drag model fit.

This model predicts that the plume will come to rest due to resistance from collisions with the background gas (see Chapter III section 3.4).

The drag model fits very well our experimental data at later time delays for all the used oxygen pressure. According to Amoruso et al. [43, 49] the plume stops when the shockwave gradually degenerates into a sound wave in the undisturbed gas, and almost all the energy initially stored in the plume (E_p) is converted into a sound wave propagating in the ambient gas. In Table 5.4, the observed plume stopping distance versus oxygen gas pressure can be evaluated from the equation of the drag model. The stopping distance decrease from 35 mm to about 20.6 mm for 0.02 and 0.8 mbar respectively.

Arnolds et al. [50] gave a more general description to the plume dynamics into background gas pressure using dimensionless distance-time variables. The model proposed describes the different stages of the plume expansion: the free expansion; the shock-wave-like expansion and finely the plume stopping. As it is illustrated in Fig. 5.21 where the data reported in Fig. 5.19 are plotted in terms of the dimensionless variables, all the curves for different pressures collapse onto an almost single one at the earlier time of propagation and where the shock wave model was valid.

As the times involve we can notice the deviation from the ideal shock wave expansion model when decreasing the pressure and this mark the interactions between the gas and the plasma plume and the formation of the shock wave along with the increase of the oxygen pressure.

159

5.5 Conclusion

The plume expansion passes from free-like to shocklike and finally reaches a complete stopping at times and distances depending on the gas pressure. It was found that the validity of the shock-wave model is restricted to a distance region which depends on the gas pressure. A drag model is a good approximation for the later plume expansion regime. Using the dimensionless variables, all of the R–t plots for the different used pressures collapse almost into a single curve. An optimal target-substrate distance was predicted for each gas pressure based on the plasma plume stopping distance.

This study on plasma expansion demonstrates the direct dependence of O_2 pressure of the evolution of the crystalline state and surface morphology of PLD grown $Sm_{0.55}Nd_{0.45}NiO_3$ films. In fact the presence of gas produces the plasma confinement and consequently an increase of the density of the ejected species (O^{2-}, Ni^3,......etc.) in the plasma, giving rise more scatterings and interactions between the O^{2-} and Ni^{3+}.

This behaviour is consistent with a slowing down of the ejected species velocity both at large distances from the target and at high gas pressures. Because of the estimated stopping distance of plume which was below the target-substrate distance used 3.0 cm and due to re-exposure of the films to the plasma, subsequent nucleation and growth of new spherical particles on the particles formed has taken place. On the basis of these data it has to be noticed that this estimate morphology feature where all films show a similar behavior as a function of pressure, can be related into the diffusion of the plasma species as the films were deposited at

161

[16]   L.Bardotti, P. Jensen, A. Hoareau, M. Treilleux, B.Chabaud, Phys. Rev. Lett. 74 (1995) 4694.

[17]   S.J. Carroll, P.D. Nellist, R.E. Palmer, S. Hobday, R. Smith, Phys. Rev. Lett. 84 (2000) 2654.

[18]   S.J Carro ll, S. Pratontep, M. Streun, R. E. Palmer, S. Hobday, R. Smith, J. Chem. Phys. 113 (2000) 7723.

[19]   M. Di Vece, S. Palomba, R.E. Palmer, Phys. Rev. B 72 (2005) 073407.

[20]   R. Smith, C. Nock, S.D. Kenny, J.J. Belb runo, M. Di Vece, S. Palomba, R.E. Palmer, Phys. Rev B 76 (2006) 25429.

[21]   N. Vandamme, E. Janssens, F. Vanhoutte, P. Lievens, C. Van Haesendonck, J. Phys.: Cond. Matter 15 (2003) S2983.

[22]   O. Rattunde, M. Moseler, A. Hafele, J. Kraft, D. Rieser, H. Haberland, J. Appl. Phys. 90 (2001) 3226.

[23]   E. Irissou, B. Le Drogoff, M. Chaker, and D. Guay, J. Appl. Phys. 94 (2003) 4796.

[24]   A.V. Bulgakov and N.M. Bulgakova, J.Phys.D: Appl.Phys. 31 (1998) 693.

[25]   S. Amoruso, A. Sambri, X. Wang, J. Appl. Phys. 100 (2006) 013302.

[26]   D.B. Geohegan, A.A. Puretzky, G. Duscher, S.J. Pennycook, Appl. Phys. Lett. 72 (1998) 2987.

[27]   D.H. Lowndes, C.M. Rouleau, T. Thundat, G. Duscher, E.A. Kenik, S.J. Pennycook, Appl. Surf. Sci. 127–129 (1998) 355.

[28]   E. Irissou, B. Le Drogoff, M. Chaker, M. Trudeau, D. Guay J. Mater. Res. 19(3) (2004) 950.

[29]   R. Dolbec, E. Irissou, M. Chaker, D. Guay, F. Rosei, M.A. El Khakani, Phys. Rev. B 70 (2004) 201406(R).

[30]   D. Riabinina, M. Chaker, F. Rosei, Appl. Phys. Lett 89 (2006) 131501.

[31]   H. Zhu, R.S. Averback, Philos. Mag. Lett. 73 (1996) 27

[43] S. Amoruso, A. Sambri, M. Vitiello, X. Wang, Appl. Surf. Sci. 252, 4712 (2006)

[44] S.S. Harilal, C.V. Bindhu, M.S. Tillack, F. Nadjmabadi, A.C. Gaeris, J. Appl. Phys. 93, 2380 (2002)

[45] A. Kushwaha, R.K. Thareja, Appl. Opt. 47, G65 (2008)

[46] P. Serra, L. Cléries, J.L. Morenza, Appl. Surf. Sci. 96–98, 216 (1996)

[47] T.E. Itina, J. Hermann, P. Delaporte, M. Sentis, Phys. Rev. E 66, 066406 (2002)

[48] Ya.B. Zel'dovich, Yu.P. Raizer, Physics of Shock Waves and High-Temperature Hydrodynamic Phenomena (Academic Press, New York, 1966)

[49] S. Amoruso, R. Bruzzesi, N. Spinelli, R. Velotta, M. Vitiello, X. Wang, Phys. Rev. B 67, 224503 (2003)

[50] N. Arnold, J. Gruber, J. Heitz, Appl. Phys. A 69, S87 (1999).

UNIVERSITY *of the*

WESTERN CAPE

165
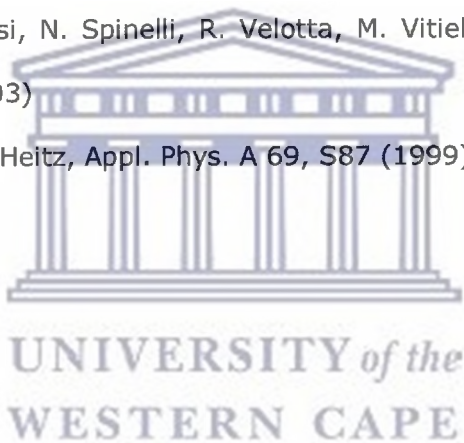
CHAPTER VI

6. CONCLUSION AND OUTLOOK

This work dealt with the study of pulsed laser deposition of complex oxides rare earth Nickelates by meanly means of three techniques, such as X-ray Diffraction technique (XRD), optical microscopy (SEM and AFM) and ICCD fast imaging. These techniques allowed investigating two main distinct aspects of pulsed laser deposition process i.e. the plume expansion and the film growth, thus highlighting the direct correlations among them.

Such correlated study provides the opportunity of gaining a deeper understanding of the effect of the various processing parameters on the final film quality, allowing a fine tailoring of the experimental conditions in view of the desired film properties.

Such quantitative approach to pulsed laser deposition is particularly relevant in the case of complex rare earth nickel oxides, since it is known that their properties can be modified in a dramatic way by minor structural tuning. Only a careful control of thin film growth can therefore allow their application in the fabrication of photonic or electronic devices. Among the wide class of complex rare earth nickel oxides, the present work focused on $Sm_{0.55}Nd_{0.45}NiO_3$ compounds. The film deposition was investigated, with respect to both the background gas pressure and the deposition time.

Our results point to the presence of an interesting cross–correlation among the deposition parameters which are usually overlooked in the usual empirical approach

shape which indicates that the laser ablation of this nickelate family is governed to a certain extent by a heat transfer phenomenon.

For an accurate description of the ablation process, a comprehensive study of the plume dynamic was required; in that line we compare the films properties and the plasma dynamic data. On the basis of these data it has to be noticed that this estimate morphology feature where all films show a similar behavior as a function of pressure, can be related into the free-expansion model which describes well the expansion of plasma on range of pressure where the films have been deposited.

It is a subject of future work to focus on Nanophotonics investigations based on nano-gold particles embedded in this rare earth nickelate type exhibiting a first order phase transition. More accurately, the pivotal advantage of the considered nano-plasmonic i.e. nano Au embedded in $Sm_{0.55}Nd_{0.45}NiO_3$ host matrix is that it exhibits a unique controllable Metal-Insulator Transition «MIT» temperature «T_{MIT}» depending on the rare earth relative atomic concentration «x».

$Sm_{0.55}Nd_{0.45}NiO_3$ can withstand extreme conditions under different external stimuli; pressure and laser fluence in particular. Hence, one should conclude that $Sm_xNd_{1-x}NiO_3$ based nano-plasmonics where the $Sm_xNd_{1-x}NiO_3$ acts as an active host matrix would display obviously a tunable and a larger 3rd order nonlinear optical susceptibility $X_3(T)$ due to local field enhancement effects as it was confirmed in the case of VO_2 based nano-plasmonics by our team. Relatively, they should endure high power laser excitations of the type of femtosecond very intense pulses owing to the high pressure-high temperature stability of the nickelate family.

The future focus of this research project is mainly to:

169